



HAL
open science

Coupled hydrogen and fluorine incorporation in garnet: New constraints from FTIR, ERDA, SIMS, and EPMA

Jed L Mosenfelder, Anette von der Handt, Anthony C Withers, H el ene
Bureau, Caroline Raepsaet, George R Rossman

► To cite this version:

Jed L Mosenfelder, Anette von der Handt, Anthony C Withers, H el ene Bureau, Caroline Raepsaet, et al.. Coupled hydrogen and fluorine incorporation in garnet: New constraints from FTIR, ERDA, SIMS, and EPMA. *The American Mineralogist*, 2022, 107 (4), pp.587 - 602. 10.2138/am-2021-7880 . hal-03748020

HAL Id: hal-03748020

<https://hal.science/hal-03748020v1>

Submitted on 9 Aug 2022

HAL is a multi-disciplinary open access archive for the deposit and dissemination of scientific research documents, whether they are published or not. The documents may come from teaching and research institutions in France or abroad, or from public or private research centers.

L'archive ouverte pluridisciplinaire **HAL**, est destin ee au d ep ot et  a la diffusion de documents scientifiques de niveau recherche, publi es ou non,  emanant des  tablissements d'enseignement et de recherche fran ais ou  trangers, des laboratoires publics ou priv es.

1 **Revision 1**

2
3 **Coupled hydrogen and fluorine incorporation in garnet: new**
4 **constraints from FTIR, ERDA, SIMS, and EPMA**
5

6
7 JED L. MOSENFELDER^{1*}, ANETTE VON DER HANDT¹, ANTHONY C. WITHERS²,

8 HÉLÈNE BUREAU³, CAROLINE RAEPSAET⁴, and GEORGE R. ROSSMAN⁵

9
10
11
12 ¹Department of Earth and Environmental Sciences, University of Minnesota, 116 Church St. SE,
13 Minneapolis, Minnesota, 55455, U.S.A.

14 ²Bayerisches Geoinstitut, Universität Bayreuth, 95440 Bayreuth, Germany.

15 ³Institut de Minéralogie, de Physique des Matériaux et de Cosmochimie (IMPMC), Sorbonne
16 Université, CNRS UMR 7590, Muséum National d'Histoire Naturelle, 4 place Jussieu, 75252
17 Paris Cedex 05, France.

18 ⁴Service de Physique de l'état Condensé, SPEC, CEA, CNRS, Université Paris-Saclay, CEA
19 Saclay, 91191 Gif sur Yvette, CEDEX, France.

20 ⁵Division of Geological and Planetary Sciences, California Institute of Technology, M/C 170-25,
21 Pasadena, California 91125-2500, U.S.A.

22
23 Word count: 13,992 (including abstract, references, and figure captions)

24 * E-mail: jmosenfe@umn.edu

25

26

27

28

ABSTRACT

29 It is well known that some garnet compositions can incorporate hydrogen and/or fluorine

30 at levels up to several weight percent. However, accurate measurement of these elements can be

31 difficult at trace to minor levels of abundance so they are frequently ignored in routine chemical

32 analysis. Furthermore, the mechanisms of H incorporation are still under debate and only one

33 mechanism for F substitution is commonly considered. We employed infrared spectroscopy

34 (FTIR), elastic recoil detection analysis (ERDA), secondary ion mass spectrometry (SIMS), and

35 electron probe microanalysis (EPMA) to measure H and F concentrations and constrain

36 incorporation mechanisms in ten grossular garnets. We also present SIMS data for 11 spessartine

37 and two andradite garnets. Three grossular garnets were measured with ERDA to obtain an

38 infrared integral molar absorption coefficient (ϵ) for H₂O of 13,470 L · mol⁻¹ · cm⁻². Grossular

39 H₂O and F concentrations range from 0.017 to 0.133 wt% and 0.012 to 0.248 wt%, respectively.

40 Correlations between ¹⁶OH and ¹⁹F and interpretation of FTIR spectra prompt us to consider

41 various coupled substitutions of H and F for Si, which can explain some high frequency IR

42 absorption bands that have been attributed previously to "hydrogrossular clusters" (variably-

43 sized clusters in which 4H substitute for Si) or to inclusions of hydrous minerals. A strong

44 correlation between ¹⁶OH and ¹⁹F in spessartine and similar high-frequency IR bands implies a

45 similar role for H-F substitution. Coupled H-F substitution is also probably relevant to some

46 andradite-rich garnets, rare pyrope from the Dora Maira massif, and some synthetic garnets.

47 Improvements in analytical methods for trace to minor H and F open up more possibilities for

48 using these elements to calculate the activities of H₂O and F-species in fluids that were in

49 equilibrium with garnet-bearing phase assemblages, as well as constraining the recycling of these
50 elements into the mantle via study of xenoliths.

51

52 INTRODUCTION

53 Considerable progress has been made in the last three decades in understanding how trace
54 amounts of hydrogen can be incorporated in nominally anhydrous minerals, and how this H
55 (most commonly incorporated as structurally bound OH⁻ groups) affects geophysical and
56 petrologic processes in the Earth and other planetary bodies. Recent work has also highlighted
57 the potential importance of trace fluorine (substituting for O²⁻) in nominally anhydrous minerals
58 (Hervig and Bell 2005; Mosenfelder et al. 2011, 2015; Beyer et al. 2012; Bernini et al. 2012;
59 Dalou et al. 2012; Mosenfelder and Rossman 2013a,b; Crépisson et al. 2014; Roberge et al.
60 2015; Grützner et al. 2017; Klemme and Stalder 2018; Yoshino and Vazhakuttiyakam 2018). In
61 the case of garnets, a diverse supergroup of minerals widely distributed in the crust and mantle of
62 the Earth, it has long been recognized that both H and F can be structurally incorporated at levels
63 up to several weight percent (see Grew et al. 2013 for review). Researchers have taken advantage
64 of this phenomenon to constrain the activities of H₂O and F-species in fluids in equilibrium with
65 garnet-bearing phase assemblages (Manning and Bird 1990; Visser 1993; Arredondo et al. 2001;
66 Chakhmouradian et al. 2008).

67 Hydrogen and/or F may in fact be almost ubiquitously present in trace to minor amounts
68 in garnets, but are commonly ignored during chemical analysis because of difficulties inherent in
69 measuring trace concentrations of light elements with commonly available techniques such as
70 electron probe microanalysis (EPMA). Note that when we specify "H₂O" or "H" concentrations

71 in this paper we are primarily referring to the equivalent in structurally bound OH⁻ groups,
72 because H is not incorporated in the form of structurally-bound H₂O groups in garnet.

73 Hydrogen can be detected easily using Fourier transform infrared spectroscopy (FTIR) in
74 transmission mode, which also provides information on incorporation mechanisms, but
75 uncertainties remain in absolute quantification using this method (Maldener et al. 2003; Rossman
76 2006). One of the best microanalytical techniques for trace F is secondary ion mass spectrometry
77 (SIMS), which is highly sensitive owing to the ionization efficiency of both ¹⁹F⁻ and ¹⁹F⁺ and has
78 benefited from technical advances that lower detection limits to less than 1 μg/g (Hauri et al.
79 2002; Koga et al. 2003; Mosenfelder et al. 2011). However, these measurements are most
80 commonly made using F-bearing glasses for calibration, which can result in working curves with
81 large uncertainties (Mosenfelder and Rossman 2013a).

82 SIMS measurements of H in garnets have primarily concentrated on pyrope-rich
83 compositions representative of the mantle (Koga et al. 2003; Aubaud et al. 2007; Tenner et al.
84 2009), with one more recent study on grossular and spessartine (Reynes et al. 2018). Quantitative
85 SIMS analyses of F in garnets are even more sparse (Jamtveit and Hervig 1994; Schingaro et al.
86 2016). In this study, we present new SIMS, FTIR, and EPMA data on the H and F concentrations
87 of ten natural grossular garnets, and SIMS data on 11 spessartine and two andradite crystals.
88 Furthermore, based on elastic recoil detection analysis (ERDA) of three grossular samples, we
89 reassess calibrations for the IR molar absorption coefficient for H₂O derived by Rossman and
90 Aines (1991) and Maldener et al. (2003). We demonstrate that H and F concentrations are
91 strongly correlated in some garnets and suggest coupled H-F incorporation mechanisms
92 analogous to those proposed for olivine by Crépeisson et al. (2014). Coupled H-F substitution can
93 rectify unexplained aspects of previous incorporation models for H in grossular, spessartine, and

94 pyrope (Aines and Rossman 1984; Rossman and Aines 1991; Cho and Rossman 1993; Reynes et
95 al. 2018; Geiger and Rossman 2018, 2020a, 2020b).

96

97

ANALYTICAL METHODS

98 **Sample selection and preparation**

99 Table 1 lists the localities of the grossular garnets chosen for this study. Six of these
100 garnets, derived from granulites of the Neoproterozoic Mozambique belt in Tanzania and Kenya
101 (Giuliani et al. 2008, 2011), are referred to as "East African" in this paper. Additional details on
102 the grossular, spessartine, and andradite samples used in the study are provided in the
103 supplementary material.

104 Samples were prepared for analysis using previously described, epoxy-free polishing
105 methods and cleaning procedures (Mosenfelder et al. 2011). The garnets were fabricated into
106 doubly polished slabs that were first measured by FTIR and then sliced using a wire saw into
107 multiple chips for analysis by different techniques; in all cases, individual chips originated from
108 the same single crystal.

109

110 **FTIR**

111 Unpolarized infrared absorption spectra were collected for most of the garnets using the
112 main compartment of either a Nicolet Magna 860 FTIR or Thermo-Nicolet iS50 FTIR at Caltech.
113 All measurements employed a GLOBAR IR source, a KBr beamsplitter, and a MCT-A detector,
114 with at least 512 scans taken at 2 cm⁻¹ resolution. Analysis areas were selected using 200 to 400
115 μm diameter circular apertures and multiple spectra for each crystal were taken to assess the
116 possibility of zoning. Sample thicknesses were measured using a Mitutoyo digital micrometer,

117 with a precision of $\pm 2 \mu\text{m}$. JLM83a was measured at UMN using a Hyperion 2000 microscope
118 attached to a Bruker Tensor 37 spectrometer, with a GLOBAR IR source, a KBr beamsplitter,
119 and a MCT-A detector. These spectra were collected on a slab $\sim 390 \mu\text{m}$ thick, with 64 scans at 2
120 cm^{-1} resolution, using a $100 \mu\text{m}^2$ square knife-edge aperture. The video-assisted mapping feature
121 of the OPUS 7.2 software was employed to take regularly spaced data (in a 6 x 8 grid) across the
122 central portion of the sample slab.

123 The low temperature (77 K) spectrum of GRR1386 was obtained in 1994 using a
124 homebuilt vacuum chamber in the main compartment of the Nicolet 60SX FTIR that was
125 operational at that time at Caltech. The room temperature spectrum of the sample taken in 1994
126 closely matches more recently acquired spectra.

127 Details of our baseline correction methods are provided in the supplementary material.
128 After baseline correction, we calculated total integrated band areas in the O-H stretching region,
129 referred to hereafter as $Ab_{s_{\text{tot}}}$ (considered here as absorbance/ cm^2 in one direction, rather than
130 multiplying one measurement by three as in some studies on garnets). Spectra were then curve
131 fitted using the Multiplex Fitting 2 package in Igor Pro software. Table 1 also gives values for
132 the weighted mean wavenumber (as defined by Libowitzky and Rossman 1997) for each
133 spectrum.

134

135 **ERDA**

136 In Table 2 we report hydrogen concentrations measured by ERDA for three grossular
137 samples (GRR732, GRR771, and GRR1756), one synthetic forsterite (GRR1017), and three
138 synthetic, rhyolitic glasses (NSL1, N3, and N5). The analyses were conducted at the Laboratoire
139 d'Etudes des Eléments Légers, CEA, Saclay, France using improved methods for micro-ERDA

140 (Raepsaet et al. 2008, Bureau et al. 2009). Analytical methods followed those outlined by
141 Withers et al. (2012) and are detailed in the supplementary material. GRR1017, well-
142 characterized as an ultra-dry reference material with $\leq 0.007 \mu\text{g/g H}_2\text{O}$ (Mosenfelder et al. 2011),
143 was used to assess the H background. Water contents of the rhyolitic glasses were previously
144 reported in Tenner et al. (2009), measured using Karl-Fischer titration as described in Withers
145 and Behrens (1999).

146

147 **SIMS**

148 SIMS data (Table 3) were obtained on the CAMECA 7f-GEO at Caltech using a Cs⁺
149 primary ion beam and previously described methods optimized for collecting low-blank H and F
150 analyses (Mosenfelder and Rossman 2013a; Mosenfelder et al. 2011, 2015). Data are presented
151 from two sessions, conducted in 2012 and 2016. For each analysis, we acquired either 30 cycles
152 (in 2012) or 20 cycles (in 2016) through the mass sequence ¹²C, ¹⁶O¹H, ¹⁸O, ¹⁹F, and ³⁰Si,
153 collecting negative ions with a mass resolution of ~ 5500 ($\Delta M/M$), sufficient to separate ¹⁶O¹H
154 from ¹⁷O and ¹⁸O¹H from ¹⁹F (Burdo and Morrison 1971). Analyses from 2012 were obtained
155 from garnets pressed into the same indium mount as the orthopyroxenes, clinopyroxenes,
156 olivines, and F-bearing glasses (MPI-DING glasses KL2-G and ML3B-G and USGS glasses
157 BCR-2G and BHVO-2G) reported on previously (and analyzed during the same session) by
158 Mosenfelder and Rossman (2013a,b). Some of the garnets were then extracted, re-polished,
159 cleaned, and pressed together into a new indium mount with one additional garnet (JLM83a), the
160 MPI-DING and USGS glasses, and five additional F-bearing glasses (Fba-1, 2, 3, 4 and 5)
161 prepared by Guggino et al. (2011). We used the Fba-series glasses to reevaluate the F
162 concentrations of our MPI-DING and USGS glass splits, as described in Mosenfelder et al.

163 (2020). The revised reference values used to establish working curves for F are given in the
164 supplementary material.
165 $^{16}\text{O}^1\text{H}/^{18}\text{O}$ and $^{19}\text{F}/^{18}\text{O}$ ratios in Table 3 were blank corrected using $^{16}\text{O}^1\text{H}$ and ^{19}F
166 backgrounds monitored by analyzing "blank" reference materials: synthetic forsterite GRR1017
167 (Mosenfelder et al. 2011), a natural Cr-rich pyrope from Ugelvik, Norway (GRR332), and
168 laboratory-dehydrated grossular (GRR1122-HT) and spessartine (GRR2215-HT). Details on
169 characterization of these samples are provided in the supplementary material.

170

171 **EPMA**

172 Electron microprobe analyses (Table 4) for most samples were acquired using a JEOL
173 JXA-8900R at UMN. We first measured F, using MgF_2 as a standard; other elements were
174 subsequently analyzed on the same spots using different analytical conditions. F $\text{K}\alpha$ was acquired
175 on three TAP crystals simultaneously and intensities were then aggregated and combined with
176 the other elements during post-processing with Probe for EPMA software (Probesoftware, Inc.).
177 Despite its lower sensitivity for F $\text{K}\alpha$, we prefer TAP over LDE1 for this application, because
178 LDE1 has the inherent problem of significant background interferences between the F $\text{K}\alpha$ and Fe
179 $\text{K}\alpha$, Mg $\text{K}\beta$, and Mn $\text{K}\alpha$ X-ray lines (e.g., Witter and Kuehner 2004; Zhang et al. 2016). We
180 found that an accelerating voltage of 20 kV optimized fluorescence yields and peak-to-
181 background ratios for F on TAP. For most of the garnets, a beam current of 250 nA and beam
182 diameter of 10 μm was used for this stage of the analysis. Analyses of JLM83a were conducted
183 at either 200, 250, or 400 nA. Calculated detection limits range from ~ 40 at the highest current to
184 60 $\mu\text{g/g}$ at the lowest current.

185 Using the procedure outlined by Donovan et al. (2011), an exponential background was
186 fit to the F $\text{K}\alpha$ peak with parameters based on a detailed wavescan of Asbestos grossular.
187 Counting times for each spectrometer were 400 seconds on peak and 350 seconds on each
188 background position, resulting in aggregated times per analysis of 1200 seconds on peak and
189 2100 seconds on the background measurement. Time-dependent intensity (TDI) loss (or gain)
190 was monitored for all elements, but no significant or systematic dependence was found so the
191 TDI correction was not used. Unknown and standard intensities were corrected for deadtime and
192 standard intensities were corrected for standard drift over time.

193 Major and minor elements were measured using an accelerating voltage of 15 kV, a beam
194 current of 20 nA, and a beam diameter of 1 μm . Counting times for each element were 20
195 seconds on peak and 10 seconds at each background position. Reference materials used for
196 calibration included synthetic forsterite (GRR1017) and tephroite (GRR392) for Mg and Mn,
197 respectively; a natural almandine (Harvard 112140) for Fe; Asbestos grossular for Ca and Si;
198 chromite (NMNH 117075) for Cr; ilmenite (NMNH 96189) for Ti; Brazilian spessartine (Verma,
199 1960) for Al; and vanadium metal for V. Na and K were also analyzed but were below the
200 detection limit in all samples.

201 Final data processing used the CITZAF matrix correction method (Armstrong 1988), with
202 FFAST mass absorption coefficients (Chantler et al. 2005). The matrix correction takes into
203 account oxygen calculated by cation stoichiometry and the oxygen equivalent from F. Cation
204 proportions (including reassignment of total Fe to Fe^{2+} and Fe^{3+}) and garnet end members were
205 calculated using the Excel spreadsheet written by Locock (2008).

206 We also report EPMA data for two samples (GRR732 and GRR1429) that were acquired
207 at Caltech using a JEOL JXA-8200. We used protocols for these analyses similar to those used at

208 UMN but did not measure F. Reference materials for calibration included synthetic pyrope for
209 Mg, Al, and Si; synthetic tephroite (GRR392) for Mn; synthetic fayalite for Fe; grossular
210 (GRR1386) for Ca; and synthetic rutile, Cr₂O₃, and V₂O₅ for Ti, Cr, and V, respectively.

211

212 **RESULTS**

213 **FTIR spectroscopy**

214 FTIR spectra representing the full variation in O-H stretching vibrations in the grossular
215 samples we studied are displayed in Figure 1. Following Rossman and Aines (1991), these
216 spectra can be separated into different classes according to the most prominent absorption bands
217 present. Class 2, represented by GRR42 (Fig. 1a), is dominated by strong peaks at 3647, 3656,
218 3676, and 3687 cm⁻¹, with the highest peak at 3647 cm⁻¹. A subset of spectral class 2 is class 2b,
219 which exhibits the same bands at high frequency (also with maximum absorbance at 3647 cm⁻¹)
220 but has multiple bands between 3600 and 3500 cm⁻¹ (Fig. 1a). Class 2b is represented by five of
221 the East African garnets (GRR229, GRR732, GRR771, GRR1386a, and GRR1386), which have
222 spectra with similar shapes but varying $Ab_{s_{tot}}$ (Table 1 and supplemental Fig. S1). Three
223 grossular garnets (GRR1122, GRR1429, and GRR1756) fall into class 7 in the Rossman and
224 Aines scheme because their strongest absorption is at 3599 cm⁻¹ rather than at 3647 cm⁻¹, but
225 otherwise their spectra are similar to class 2b; class 2b and class 7 are compared on the same
226 scale in Figure 1b.

227 The Asbestos garnet JLM83a (Fig. 1c) is typical of class 3, with a strong peak at 3631
228 cm⁻¹ that is not as prominent in the other garnets. JLM83a also has bands centered at ~3621,
229 3644, 3659, 3665, 3677, and 3689 cm⁻¹. Garnets from Asbestos fall into both classes 3 and 4,
230 where class 4 is defined by having its strongest peak at 3621 cm⁻¹. Figure 1c compares spectra of

231 JLM83a to published spectra of some other Asbestos grossular garnets (GRR53 and GRR1537)
232 and end-member grossular crystals synthesized by Geiger and Armbruster (1997) and Withers et
233 al. (1998).

234 Whereas the absorbance among different East African grossular varies widely (Table 1
235 and supplemental Fig. S1), we failed to detect H zoning within any individual single crystal from
236 this area. The only crystals in our study that are significantly zoned, based on FTIR, are JLM83a
237 and GRR1429. $Ab_{s_{tot}}$ in JLM83a varied by a factor of ~ 2 in the range between 3750 and 3300
238 cm^{-1} . All spectra have similar shapes, but relative intensities of the peaks at 3631 and 3621 cm^{-1}
239 vary (Fig. 1c). Rossman and Aines (1991) noted a comparable variation in $Ab_{s_{tot}}$ for GRR53,
240 from the same locality. Systematic zoning patterns (such as core-rim relationships or sector
241 zoning) could not be deciphered in the randomly cut slab of JLM83a that we used for both FTIR
242 and SIMS measurements. Although variations in absorbance in Asbestos garnets have been
243 attributed previously to birefringence (Rossman and Aines 1986; Allen and Buseck 1988), our
244 SIMS measurements (Table 3 and discussion below) demonstrate that actual differences in H
245 concentration are a more important factor in this crystal.

246 GRR1429 is also birefringent, which might be the cause of the variations in $Ab_{s_{tot}}$ (about
247 5% relative) in this sample. We used the average of seven baseline-corrected, unpolarized
248 spectra taken on separate spots to estimate its H_2O content.

249 Close examination of the spectrum of GRR1386 (Fig. 1a) reveals 12 peaks between 3700
250 and 3500 cm^{-1} and the shoulders on some of the bands indicate that curve fitting should take into
251 account more than 12 bands. Figure S5 in the supplementary material displays an example of
252 curve fitting for this garnet. We fit 15 bands with a pseudo-Voigt profile (mixed Gaussian and
253 Lorentzian), at 3531, 3539, 3546, 3567, 3583, 3599, 3608, 3623, 3631, 3643, 3647, 3657, 3664,

254 3674, and 3688 cm^{-1} . Although the fit is obviously non-unique, our peak positions (with initial
255 guesses based on visual examination) are within 1 cm^{-1} of those fit for the same sample by
256 Geiger and Rossman (2020a), with the slight difference that we fit an additional band at 3539
257 cm^{-1} not present in their fit. We used these peak positions as a basis to fit spectra for the other
258 grossular garnets. Fitted peak centers in other samples are mostly within 1 cm^{-1} of those for
259 GRR1386, with a few deviations up to 3 cm^{-1} . A table with the fit results for all samples is
260 provided in the supplementary material.

261 The cooling experiment conducted on GRR1386 demonstrates that nearly all the mid-IR
262 absorption in this garnet can be attributed to structurally incorporated O-H, with most bands
263 shifting to higher energies upon cooling to 77 K (Fig. 2). There is no evidence for band splitting
264 at low T , as observed in many other garnets (Geiger et al. 1991; Geiger and Rossman 2018).
265 However, enlargement of the baseline region reveals a broad absorption band at $\sim 3400 \text{ cm}^{-1}$ that
266 shifts to $\sim 3240 \text{ cm}^{-1}$, typical of the transition from liquid water to ice (also plotted for
267 comparison in Fig. 2 are spectra for water and ice from Bertie and Lan 1996 and Johnson and
268 Rossman 2003). The 3400 cm^{-1} band is apparently also present in some of the other garnets, but
269 quantification is hampered by high-frequency interference fringes in most spectra (not visible at
270 the scales used in Fig. 1). The liquid water in GRR1386 is probably contained in sub-micrometer
271 sized fluid inclusions, as found in other NAMs (e.g., Johnson and Rossman 2003; Mosenfelder et
272 al. 2011). Its contribution to $Ab_{S_{\text{tot}}}$ for this sample amounts to 1.2%. We have elected not to
273 correct any of the estimates for $Ab_{S_{\text{tot}}}$ in Table 1 for the possible presence of H_2O . Furthermore,
274 we have ignored another possible contribution to $Ab_{S_{\text{tot}}}$ in the O-H stretching region from the
275 lowest energy spin-allowed Fe^{2+} transition in grossular with FeO content greater than 1 wt%
276 (GRR42, GRR1122, GRR1386a, GRR1429, and JLM83a). This band should occur at lower

277 energy compared to other garnets (Geiger and Rossman 1994), because the larger size of the X
278 cation site in grossular leads to greater splitting of the Fe²⁺ bands (White and Moore 1972).
279 However, its exact position is difficult to determine owing to superposition of O-H stretching
280 vibrations (Slack and Chrenko 1971; White and Moore 1972).

281

282 **ERDA**

283 H₂O concentrations of the three grossular garnets, three rhyolitic glasses, and dry
284 forsterite as determined by ERDA are given in Table 2. ERDA and PIXE detector maps of the
285 analyzed areas for two of the garnets (GRR1756 and GRR732) revealed no significant
286 heterogeneities, but a small, anomalous region of interest with high H and Ca content in GRR771
287 was excluded in the calculation of its bulk H content. This "hot spot" probably represents surface
288 contamination (Withers et al. 2012). Bulk H (ERDA) and Ca (PIXE) maps for this sample are
289 provided in the supplementary material.

290 The nominal H₂O concentration measured by ERDA in GRR1017 forsterite, established
291 as an ultra-dry "blank" material with $\leq 0.007 \mu\text{g/g H}_2\text{O}$ (Mosenfelder et al. 2011), is 101 ± 14
292 $\mu\text{g/g}$. The bulk H concentrations for grossular are strongly correlated with $Ab_{s_{tot}}$ (Fig. 3). We
293 applied a York regression to the data (York et al. 2004; Vermeesch 2018), taking into account
294 uncertainties in both $Ab_{s_{tot}}$ and the ERDA measurements. The regression yields an intercept of
295 $100 \pm 13 \mu\text{g/g H}_2\text{O}$, which is the value we subtract to arrive at the blank-corrected H₂O
296 concentrations. The slope of the fit line provides the following calibration for infrared
297 measurements:

298

$$299 \quad C_{\text{H}_2\text{O}} (\mu\text{g/g}) = 0.370 (\pm 0.035, 2\sigma) \times Ab_{s_{tot}} \quad (1)$$

300

301 The integral molar absorption coefficient (ϵ , in $\text{L} \cdot \text{mol}^{-1} \cdot \text{cm}^{-2}$) can be derived by substituting
302 the above relation into a modified form of the Beer-Lambert law (e.g., Johnson and Rossman,
303 2004),

304

$$305 \quad C_{\text{H}_2\text{O}} (\mu\text{g/g}) = Abs_{tot} \times 18.015 \times 10^6 / [\rho \cdot \epsilon_i], \quad (2)$$

306

307 where ρ is the density of the mineral (in g/L , or kg/m^3). Assuming for simplicity a typical density
308 for V-bearing grossular of 3615 kg/m^3 (Maldener et al. 2003), we derive a value for ϵ_i of $13,470$
309 $\text{L} \cdot \text{mol}^{-1} \cdot \text{cm}^{-2}$.

310 A check on the accuracy of our ERDA data on grossular is provided by the results on the
311 three rhyolitic glasses, which are in excellent agreement with previously published total H_2O
312 concentrations determined for these samples using Karl-Fischer titration (Tenner et al. 2009).
313 The H_2O contents of the glasses measured by ERDA are within 5% of the reference values.

314

315 **SIMS and EPMA measurements of H and F**

316 SIMS data for the sessions conducted in 2012 and 2016 are summarized in Table 3, with
317 complete data for all individual analyses provided in the supplementary material. Statistics are
318 reported in this paper using the symbology of Fitzsimons et al. (2000). Internal precision in
319 $^{16}\text{OH}/^{18}\text{O}$ (calculated from $2s_{\bar{x}}$, the standard error of the mean for 20 or 30 cycles through the
320 mass sequence) ranged from 0.24 to 1.35% relative for all garnets except GRR1122-HT (the
321 blank) and JLM83a. Measured $^{19}\text{F}/^{18}\text{O}$ ratios were similarly precise (0.15 to 0.52%). The high

322 variability in internal precision as well as external precision (reproducibility) for JLM83a is
323 discussed below.

324 $^{16}\text{OH}/^{18}\text{O}$ for each garnet with the exception of JLM83a is plotted in Figure 4 as a
325 function of H_2O concentration determined from FTIR data using the ERDA calibration. Similar
326 plots are derived if ^{30}Si is used instead of ^{18}O as the reference mass. Uncertainties in H_2O
327 concentration were estimated by propagating the error in Abs_{tot} (Table 1) and the uncertainty in
328 the fit to the ERDA data (Fig. 3 and Equation 1). York regressions applied to the data for East
329 African garnets (GRR229, GRR732, GRR771, GRR1386, GRR1386a, and/or GRR1756) have
330 indistinguishable slopes for the two sessions. These regressions also fit well to the data for
331 GRR1429 and GRR1122 measured in 2012. However, the 2016 data for GRR1122 are
332 significantly offset from the regression line, as are both the 2012 and 2016 data for GRR42.

333 In the case of GRR1122 we provisionally attribute this discrepancy to heterogeneity in
334 the sample not recognized from FTIR data and insufficiently probed by the six SIMS analyses
335 that were acquired. The heterogeneity could be related to the presence of fluid inclusions,
336 indicated by a weak broad band at 3420 cm^{-1} similar to that seen in GRR1386 (Fig. 2). As for
337 GRR42, the consistency in values for seven analyses from the two sessions suggests a different
338 explanation for the offset from the regression. In the discussion section, we explore the
339 possibility that the H concentration of GRR42 is significantly underestimated owing to the
340 frequency dependence of the IR molar absorption coefficient, which cannot be accurately
341 constrained from our ERDA data.

342 Fluorine concentrations measured by SIMS and EPMA are compared in supplemental
343 Figure S8. The SIMS concentration values are tied to our redetermination of reference values for
344 the F-bearing basaltic glasses we regularly use for calibration, not taking into account any

345 possible SIMS matrix effect. The close correspondence between SIMS and EPMA values (with
346 all values reasonably close to the 1:1 line) suggests that any such matrix effect is minimal in this
347 case.

348 The heterogeneity in apparent H₂O concentrations measured by FTIR in JLM83a was
349 confirmed by the grid map of SIMS analyses taken over approximately the same area (Fig. 5).
350 The SIMS analyses also reveal heterogeneity in F, which was additionally confirmed by EPMA
351 (see supplementary material). The measurements using SIMS, FTIR, and EPMA cannot be
352 compared directly to determine a zoning pattern because the FTIR analyses are taken in
353 transmission, whereas the SIMS and EPMA measurements sample a volume that is close to the
354 surface (~1-2 μm deep for SIMS, and ~3 μm deep for EPMA at the analytical conditions used).
355 However, the range in apparent H₂O concentrations measured by FTIR (256-571 μg/g) is similar
356 to the range measured by SIMS (170-576 μg/g), calculated by applying the York regression in
357 Figure 4b. For the sake of this comparison we discard four analyses (marked by asterisks in Fig.
358 5) that were affected by the spike in background contaminant levels in the vacuum caused by the
359 cold trap running out of liquid N₂ (see supplementary material). These analyses had ¹²C/¹⁸O
360 ratios one to two orders of magnitude higher than the other analyses.

361 Following the 2012 session, it became apparent that ¹⁹F and ¹⁶OH are correlated for
362 some grossular garnets, particularly the East African samples with similar class 2b and class 7
363 FTIR spectra (Fig. 6a). A similar correlation was noted for spessartine (Fig. 6b). An even more
364 robust correlation exists for the data taken on JLM83a alone (Fig. 6a). The values in Figure 6a
365 for JLM83a represent average ¹⁶OH/¹⁸O and ¹⁹F/¹⁸O for each analysis. However, the internal
366 precision of the analyses varies widely, with $s_{\hat{x}}/\hat{s}_{\hat{x}}$ (where $\hat{s}_{\hat{x}}$ is the precision predicted by
367 Poisson statistics; Fitzsimons et al., 2000), ranging from 1 (ideal) to 30 (poor). We would

368 normally discriminate against SIMS measurements with such high $s_{\bar{x}}/\hat{s}_{\bar{x}}$ values; for instance, in
369 Mosenfelder et al. (2011) all analyses of olivine with $s_{\bar{x}}/\hat{s}_{\bar{x}} > 5$ were filtered out. High $s_{\bar{x}}/\hat{s}_{\bar{x}}$ in
370 olivine and orthopyroxene has been attributed to the presence of sub-micrometer to micrometer-
371 sized inclusions of hydrous minerals (such as serpentine and amphibole) and/or fluid inclusions
372 (Mosenfelder et al. 2011; Mosenfelder and Rossman 2013a). In the present case, however, we
373 attribute the high variability to zoning in H and F within the garnet itself. Analyses with high
374 $s_{\bar{x}}/\hat{s}_{\bar{x}}$ show strong cycle-to-cycle covariation between ^{19}F and ^{16}OH (Supplementary Fig. S8),
375 indicating that F and H are coupled on a sub-micrometer scale.

376

377

DISCUSSION

378 Molar IR absorption coefficient for H₂O in grossular

379 In Figure 7, we compare our ERDA data to H₂O concentrations measured (as a function
380 of $Ab_{s_{\text{tot}}}$) in grossular-rich garnets using other "absolute" techniques: NRA (Rossman and Aines
381 1991; Maldener et al. 2003), P₂O₅ cell coulometry using a moisture evolution analyzer (MEA,
382 Aines and Rossman 1984), H manometry (Aines and Rossman 1984), and continuous-flow mass
383 spectrometry (O'Leary et al., 2007). Also displayed in the graph is the regression line for all of
384 the data considered by Rossman and Aines (1991) for grossular and hydrogrossular with up to
385 12.75 wt% H₂O (with H₂O contents on the high end well-constrained using X-ray diffraction).

386 We have no definitive explanation for the discrepancy between H concentrations
387 measured in GRR732 by ERDA (599 $\mu\text{g/g}$ H₂O) and continuous-flow mass spectrometry
388 (CFMS; 1062 $\mu\text{g/g}$ H₂O); we can only speculate that the blank for that particular CFMS
389 measurement was higher than recognized. Our data show excellent agreement, however, with
390 some of the NRA data. In particular, the analyses by Maldener et al. (2003) on their TSAV (480

391 $\pm 40 \mu\text{g/g H}_2\text{O}$) and thin (0.0165 cm) slab of HESS1 ($870 \pm 90 \mu\text{g/g H}_2\text{O}$) samples lie close to
392 our regression line. These East African grossular garnets have IR spectra similar to those from
393 the same area that we measured with ERDA. Our data are in poorer agreement with Maldener et
394 al.'s analyses of a thicker (0.0312 cm) slab of HESS1 ($950 \pm 80 \mu\text{g/g H}_2\text{O}$) and with MALI (170
395 $\pm 20 \mu\text{g/g H}_2\text{O}$) and GRMALI ($190 \pm 20 \mu\text{g/g H}_2\text{O}$). The two NRA measurements of HESS1 are
396 in agreement with each other within mutual uncertainties, which suggests that there is a
397 discrepancy in the FTIR measurements (e.g., non-linearity of the detector for linear absorbance
398 higher than 1.5 in the thick HESS1 sample) or perhaps unrecognized H zoning in the crystal. The
399 discrepancies between our measurements and those on MALI and GRMALI might derive from
400 errors made in correcting the sample thicknesses for beam convergence in the microscope.
401 Furthermore, any inaccuracies in blank correction are also more likely to affect these low H
402 content samples.

403 The H concentrations of Asbestos grossular garnets GRR53 and GRR53F were measured
404 using three different techniques: H manometry, MEA, and NRA (Aines and Rossman 1984;
405 Rossman and Aines 1991). The poor agreement of our data fit with the values determined with
406 those techniques might be related to H zoning comparable to that in JLM83a. Hydrogen
407 manometry and MEA are bulk methods that sample a much larger volume than the FTIR
408 measurements and thus cannot account for fine-scale zoning. Even though NRA is a near-surface
409 technique, the beam size employed at that time was much larger (several mm) than the apparent
410 scale of H zoning in Asbestos grossular. Furthermore, the NRA measurement of GRR53F
411 employed a reaction with ^{19}F ions that was subsequently abandoned in favor of a more
412 reproducible reaction employing a ^{15}N beam (Rossman 2006).

413 There is a large discrepancy (Fig. 7) between our data fit on relatively low H content
414 grossular and the regression applied by Rossman and Aines (1991), which was largely
415 constrained by hydrogrossular garnets with high H contents. The discrepancy cannot be
416 attributed to the lower sample density of hydrogrossular; for instance, using Equation 2,
417 Crestmore hydrogrossular GRR1358, which has 12.75 wt% H₂O, $Ab_{s_{tot}}$ of 158,750 cm⁻², and a
418 calculated density of 3050 kg/m³ (Basso et al. 1983), would have an ϵ_i of 7354 L · mol⁻¹ · cm⁻²,
419 lower than our new value by a factor of almost two. The data on hydrogrossular samples could
420 have been compromised by uncertainties in sample thickness or unrecognized H zoning, but
421 these factors are speculative and more work is needed to ascertain the reason for the large
422 apparent difference between low-H grossular and hydrogrossular.

423 The possibility of a difference in calibration factor for grossular and hydrogrossular was
424 already noted by Rossman and Aines (1991), and Rossman (2006) recommended a calibration
425 factor for low H content grossular of 0.14 (for absorbance in three directions). That value,
426 equivalent to 0.42 for the convention for $Ab_{s_{tot}}$ used in this study, compares reasonably well to
427 our new value of 0.370 ± 0.035 (Equation 1). We conclude that our new calibration is more
428 appropriate than the Rossman and Aines calibration for grossular with less than ~1 wt% H₂O.

429 Empirical and theoretical studies consistently show an increase in ϵ_i with decreasing
430 frequency for O-H absorption bands (Paterson 1982; Libowitzky and Rossman 1997; Balan et al.
431 2008; Mosenfelder et al., 2015). This means that an IR calibration based on grossular with
432 relatively low mean wavenumber might underestimate the H₂O contents of grossular with higher
433 mean wavenumber. Whereas our ERDA calibration was performed on grossular with mean
434 wavenumbers between 3595 and 3622 cm⁻¹ (Table 1), GRR42 is dominated by bands with
435 significantly higher frequency (with a mean wavenumber of 3647 cm⁻¹; Fig. 1a, Table 1). A

436 frequency dependence to ϵ_i can therefore explain the offset of SIMS data for this sample in
437 Figure 4, but the magnitude of the dependence is poorly constrained. For the sake of calculating
438 formula units and garnet end-members (Table 4), we assume a H₂O concentration for this sample
439 based on the York regression shown in Figure 4a. Further work is needed to constrain the
440 frequency dependence of ϵ_i to determine whether this assumption is justified. Our calibration
441 also might underestimate H₂O concentrations for JLM83a and other Asbestos grossular garnets,
442 which also have a higher mean wavenumber (Table 1). Unfortunately, the zoning in some (or
443 all?) of these class 3 and 4 garnets will make this goal challenging, and class 2 garnets with
444 spectra like that of GRR42 are rare in our experience. A better way forward might entail
445 synthesizing grossular crystals at high *P-T* (Geiger and Armbruster 1997; Withers et al. 1998)
446 and establishing their homogeneity using a technique such as ERDA.

447

448 **Previous models of H and F incorporation mechanisms**

449 Hydrogen incorporation in garnets is classically assumed to take place via the
450 "hydrogarnet" substitution, whereby four H atoms bond to the O atoms surrounding a vacant Si
451 site. Hereafter, we refer to this substitution as $(4H)_{Si}^{\times}$, which is a commonly used, abbreviated
452 form of the following defect associate written in Kröger-Vink (1956) notation:

453



455

456 Here, *V* represents a vacancy; the superscripts \times , \cdot and \prime represent null, positive, and negative
457 charges relative to the perfect structure, respectively; and the subscripts refer to Si and O
458 crystallographic sites. We recognize that some mineralogists might object to using point defect

459 symbolism to refer to both trace and high concentrations of elements, but we use it in the
460 following discussion for the sake of convenience.

461 The $(4H)_{Si}^x$ mechanism is well established for H-rich garnets along the grossular-katoite
462 join (for review, see Beran and Libowitzky 2006; Grew et al. 2013; and Geiger and Rossman
463 2020a), not only from chemistry but from NMR, X-ray diffraction (XRD), and neutron
464 diffraction (Cohen-Addad et al. 1987; Lager et al. 1987, 1989; Cho et al. 1993). An analogous
465 substitution of four F atoms substituting for O surrounding a vacant Si site is well documented
466 for F-rich garnets, based on XRD (Smyth et al. 1990; Chakhmouradian et al. 2008) and negative
467 correlations between Si and F concentrations (Flohr and Ross 1989; Visser 1993;
468 Chakhmouradian et al. 2008). This substitution can be written as:

469

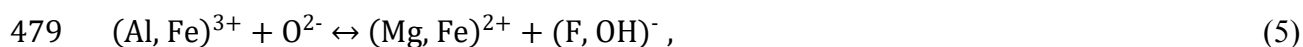


471

472 This substitution differs structurally from $(4H)_{Si}^x$ in the sense that F atoms can occupy the
473 regular site of O atoms, whereas the H atoms in $(4H)_{Si}^x$ are bonded to O that is displaced from its
474 normal position owing to expansion of the tetrahedron (e.g. Lager et al. 1989).

475 Other substitution mechanisms for H and particularly for F in garnet have received
476 somewhat less attention. Valley et al. (1983) considered the possibility, in addition to
477 mechanisms (3) and (4), of F and H incorporation in grossular via the coupled substitution:

478



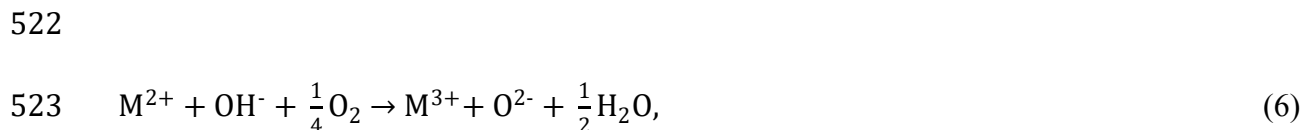
480

481 where the cations are located in the six-coordinated Y site. They recognized that verification of
482 this substitution relies on accurate determination of $\text{Fe}^{2+}/\text{Fe}^{3+}$ as well as H and F content, beyond
483 the scope of their study. Various mechanisms involving coupled substitution of Ti and H have
484 also been considered, primarily for pyrope (Bell and Rossman 1992; Khomenko et al. 1994;
485 Geiger et al. 2000) but also for grossular (Reynes et al. 2020). Partial substitution of H for the Y-
486 cation in a hydrogrossular was inferred by Kalinichenko et al. (1987), based on NMR, and at
487 least two studies have inferred substitutions other than $(4\text{H})_{\text{Si}}^{\times}$ in H-rich garnets based on crystal
488 chemical arguments (Birkett and Trcienski 1984; Basso and Cabella 1990). In principle OH^- or
489 F^- can replace O in the dodecahedral X-site in garnet, if it is vacant or contains a monovalent
490 cation (e.g., Andrut et al. 2002). For instance, a Ca vacancy in grossular can be compensated by
491 two H, which we notate as $(2\text{H})_{\text{Ca}}^{\times}$. A similar substitution for the Y cation can be notated as
492 $(3\text{H})_{\text{Al}}^{\times}$ or $(3\text{H})_{\text{Fe}}^{\times}$, depending on the garnet composition.

493 Early on in the study of nominally anhydrous minerals it was recognized that the mid-IR
494 spectra of some garnets are incompatible with the $(4\text{H})_{\text{Si}}^{\times}$ mechanism, because too many peaks
495 are present (Aines and Rossman 1984). The $(4\text{H})_{\text{Si}}^{\times}$ substitution *sensu stricto* (cf. Geiger and
496 Rossman 2020a; see below) can result in a maximum of four O-H stretching vibrations, or two if
497 the symmetry of the garnet is maintained (Harmon et al. 1982; Aines and Rossman 1984). The
498 IR spectra of many pyrope, almandine, and andradite garnets are dominated by a broad,
499 asymmetric band that splits into two bands at low temperature (cooled by liquid N_2), thus
500 consistent with $(4\text{H})_{\text{Si}}^{\times}$ (Geiger et al. 1991; Geiger and Rossman 2018). Differences in band
501 positions as a function of composition can be explained by the presence of different neighboring
502 X and Y cations, and the broad width of the bands can be explained by a combination of proton
503 disorder and variations in local cation configuration. On this basis, Geiger and Rossman (2018)

504 assigned bands at 3629, 3613, 3598, and 3563 cm^{-1} in pyrope, almandine, grossular, and
505 andradite respectively to $(4\text{H})_{\text{Si}}^{\times}$. However, in grossular, as well as many spessartine garnets
506 (Aines and Rossman 1984; Arredondo et al. 2001) and some rare pyrope garnets from the Dora
507 Maira massif (Rossman et al. 1989), the multitude of sharp peaks cannot be explained by this
508 mechanism alone.

509 Additional constraints on H incorporation in grossular and garnets on the grossular-
510 andradite join come from experimental studies of H diffusion (Kurka et al. 2005;
511 Phichaikamjornwut et al. 2012; Reynes et al. 2018). All of these studies support the idea that
512 there are multiple sites for O-H incorporation, because various O-H bands decrease at different
513 rates during dehydration. In general, dehydration kinetics for bands at higher frequency have a
514 lower activation energy (E_a) than those at low frequency. For instance, Reynes et al. (2018)
515 measured E_a for a grossular-rich garnet in the range between 157 and 185 kJmol^{-1} for bands at
516 3628, 3645, 3657, and 3686 cm^{-1} , and in the range between 216 and 275 kJmol^{-1} for bands at
517 3533, 3576, and 3604 cm^{-1} . A positive dependence of the diffusion coefficient on f_{O_2} as well as
518 observations of color changes in sample rims in the experiments by Reynes et al. also support a
519 key role for Fe^{2+} in dehydration. Reynes et al. identify a fast diffusion mechanism, analogous to
520 that identified in many other nominally anhydrous minerals (Ingrin and Blanchard 2006), that is
521 limited by the availability of Fe^{2+} :



525 where M represents either Fe or Mn, which may or may not be directly tied to a defect
526 responsible for incorporating H. Our failed attempt to fully dehydrate GRR1122 (supplementary

527 Fig. S4) at low f_{O_2} (with virtually no change in spectra between dehydration steps 1 and 2) is
528 consistent with this interpretation. We will return to this point when we discuss our model for
529 coupled H-F substitution in the next section.

530 Another critical constraint on H incorporation in grossular comes from the study of Cho
531 and Rossman (1993), who performed solid-state ^1H NMR measurements on a synthetic end-
532 member katoite ($\text{Ca}_3\text{Al}_2\text{Si}_2(\text{OH})_{12}$) powder and single crystals of GRR1386 (Fig. 1a), GRR53
533 (Fig. 1c), and GRR1537 (Fig. 1c). From their analysis of multiple-quantum spectra, Cho and
534 Rossman concluded that the protons in katoite occur in closely spaced groups of four, as
535 expected for $(4\text{H})_{\text{Si}}^{\times}$. However, the best fit to the multi-quantum spectrum of GRR1386 was for a
536 cluster size of two protons, and the best fit to the data for GRR1537 was for two separate clusters
537 consisting of two and four protons each. The class 4 IR spectrum of GRR1537 is dominated by a
538 band at 3621 cm^{-1} (Fig. 1c), which is the position of the main band in a synthetic hydrogrossular
539 with composition $\text{Ca}_3\text{Al}_2(\text{SiO}_4)_{2.28}(\text{O}_4\text{H}_4)_{0.72}$ (Rossman and Aines 1991). Therefore, Cho and
540 Rossman assigned this band to $(4\text{H})_{\text{Si}}^{\times}$ and other, less intense bands to a different, unspecified
541 defect containing two closely spaced protons.

542 Geiger and Rossman (2020a, 2020b) offered a novel explanation for the sharp, high-
543 frequency bands in natural grossular. They hypothesized that bands at 3599, 3612, 3622, 3634,
544 and 3641 cm^{-1} correspond to clustered groups of $(4\text{H})_{\text{Si}}^{\times}$ with cluster sizes of one, two, three, four
545 and five, respectively. A band at 3657 cm^{-1} was tentatively assigned to a cluster size of six, and a
546 band at 3660 cm^{-1} was assigned to a "finite size katoite cluster" based on the fact that the main
547 absorption in pure katoite (GRR1059; mislabeled as "Si 2.28" in Fig. 7 of Geiger and Rossman
548 2020a) occurs at this frequency (Rossman and Aines 1991). Bands at 3674 and 3688 cm^{-1} were

549 attributed to inclusions of hydrous minerals. This model explains all the features in IR spectra of
550 class 2, 3, and 4 grossular and all absorptions above $\sim 3600\text{ cm}^{-1}$ in class 2b.

551 It is well known from studies of hydrous minerals that the strengths of O-H bonds (and
552 thus their vibrational frequencies) are affected by different cations sharing bonds with the same
553 O atom (i.e., second nearest neighbors to the H atom). For example, the frequencies of O-H
554 bonds in amphibole, which vary by up to $\sim 50\text{ cm}^{-1}$, can be reliably assigned to different cation
555 environments (e.g., Burns and Strens 1966). Recent work has also explored the effects of
556 neighboring cations on O-H stretching frequencies in olivine (Blanchard et al. 2017). The cluster
557 model of Geiger and Rossman (2020a,b), however, relies on an assumption that comparable
558 shifts in O-H bond frequencies are influenced by bonds in other $(4\text{H})_{\text{Si}}^{\times}$ that are not directly
559 adjacent, because the tetrahedra in garnet are isolated from each other. Geiger and Rossman
560 justify this assumption as a consequence of the increase in Ca-O bond lengths between the end
561 members grossular (Geiger and Armbruster 1997) and katoite (Lager et al. 1987). It remains to
562 be shown by first-principles modeling or other methods whether or not this relaxation in Ca-O
563 distances for the end members also operates on a localized scale within small, isolated clusters of
564 $(4\text{H})_{\text{Si}}^{\times}$ in garnets with trace amounts of H. It should also be noted that the model of Geiger and
565 Rossman ignores the results of Cho and Rossman (1993) that indicate some grossular garnets
566 contain a significant fraction of defects with only two protons. Furthermore, the assignment of
567 bands at 3674 and 3688 cm^{-1} to inclusions of hydrous phases is problematic, owing to geological
568 and spectroscopic reasons that we elaborate in the supplementary material. In the following
569 sections, we offer alternative explanations for some of the absorption bands that call on coupled
570 H and F substitution for Si as well as substitution of H (and possibly F) for cations in octahedral
571 and/or dodecahedral sites.

572

573 **Coupled substitution of H and F**

574 Our first clue that incorporation mechanisms of H and F in grossular might be entangled
575 came from correlations between ^{16}OH and ^{19}F in grossular (Fig. 6a) and spessartine (Fig. 6b),
576 prompting us to consider coupled substitution of H and F for Si (or other cations). While it is
577 possible that these correlations are coincidental and reflect nothing about coupled H-F
578 substitution, interpretation of the IR spectra combined with quantitative data on H and F
579 concentrations (Table 4) suggests otherwise.

580 Consider first the comparison between GRR42 and GRR1386: these crystals have the
581 same F content (0.25 wt%), but GRR1386 has nearly twice as much H_2O (0.13 wt%) as GRR42
582 (0.07 wt%; based on SIMS). The other obvious difference (Fig. 1a) is that both garnets have
583 significant absorbance above $\sim 3620\text{ cm}^{-1}$, but GRR42 has much lower absorbance at lower
584 frequencies. This suggests that some of the high-frequency bands are related to defects
585 containing both H and F, unless all F is bound in anhydrous defects (e.g., via Equation 4). We
586 draw a similar conclusion from the comparison between GRR732 and GRR1122 in Figure 1b:
587 these garnets have nearly the same H_2O content (0.052-0.054 wt%), but GRR732 has almost
588 twice as much F (0.11 wt%) as GRR1122 (0.06 wt%) and has stronger absorbance above ~ 3620
589 cm^{-1} , whereas GRR1122 has stronger absorbance at lower frequencies. Furthermore, the
590 strongest correlation between ^{16}OH and ^{19}F is evident in JLM83a, which has virtually no
591 absorbance at frequencies lower than $\sim 3600\text{ cm}^{-1}$ (Fig. 1c) – again suggesting that the higher-
592 frequency O-H bands are related to F incorporation. An attempt to quantify these general
593 observations is summarized in Figure 8, where we plot F (per formula unit, Table 4) against the
594 band areas derived by spectral curve fitting for nine out of ten of the grossular garnets in the

595 study (JLM83a is excluded from this analysis because it is difficult to compare any given
596 spectrum to a precise F content in this zoned garnet).

597 Motivated partly by these observations and partly by the experiments and first-principles
598 density functional theory (DFT) calculations of Crépisson et al. (2014) on forsterite, we propose
599 that some of the bands at frequencies $> 3600 \text{ cm}^{-1}$ represent coupled H-F substitution for Si.
600 Following Cho and Rossman (1993) and Withers et al. (1998), we start with the assumption that
601 the band at 3621 cm^{-1} , with a shoulder at $\sim 3610 \text{ cm}^{-1}$, represents $(4\text{H})_{\text{Si}}^{\times}$. The asymmetry of the
602 stretching vibration in this region is consistent with the band structure in other garnet
603 compositions previously assigned to $(4\text{H})_{\text{Si}}^{\times}$ (Geiger and Rossman 2018), although the bands in
604 grossular are narrower. Some or all of the bands at higher frequencies are then assigned to defect
605 associates involving both OH^- and F^- :

606
607
$$\{V_{\text{Si}}^{\text{IV}} - (\text{OH})_{\text{O}}^{\cdot} - 3(\text{F})_{\text{O}}^{\cdot}\}^{\times} \quad (7)$$

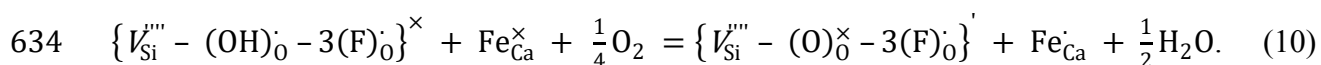
608
$$\{V_{\text{Si}}^{\text{IV}} - 2(\text{OH})_{\text{O}}^{\cdot} - 2(\text{F})_{\text{O}}^{\cdot}\}^{\times} \quad (8)$$

609
$$\{V_{\text{Si}}^{\text{IV}} - 3(\text{OH})_{\text{O}}^{\cdot} - (\text{F})_{\text{O}}^{\cdot}\}^{\times} \quad (9)$$

610
611 Calculations made by Crépisson et al. (2014) indicate that some of these clumped OH-F
612 defects in forsterite lead to O-H vibrations at higher frequencies than those assigned by previous
613 studies to the $(4\text{H})_{\text{Si}}^{\times}$ defect. For instance, the single O-H stretching vibration corresponding to
614 defect (7) is at 3674 cm^{-1} , as opposed to the four O-H vibrations predicted for the most stable
615 $(4\text{H})_{\text{Si}}^{\times}$ configurations, which are between ~ 3400 and 3625 cm^{-1} (Balan et al. 2011; Umemoto et
616 al. 2011). In general, the frequencies of bands assigned to the various clumped OH-F defects
617 decrease as the number of F atoms decreases, but complexities arise owing to the three non-

618 equivalent crystallographic sites for O in the olivine structure. A positive frequency shift is also
619 predicted for a clumped OH-F defect in an octahedral site, compared to a fully protonated
620 vacancy. The positive O-H frequency shifts for sites where F⁻ replaces O²⁻ are presumably a
621 consequence of the influence of F⁻ (which is more electronegative than O²⁻) on the geometry of
622 the polyhedron (Crépeisson et al. 2014). The theoretically derived frequencies of the clumped
623 OH-F defects represented by Equations 7-9 are consistent with IR spectra of natural olivines
624 known to contain relatively high F concentrations (Sykes et al. 1994; Libowitzky and Beran
625 1995; Mosenfelder et al. 2011), which have bands at 3670, 3637, and 3620 cm⁻¹ that are not
626 present in olivines with lower F contents.

627 Precise assignment of individual high-frequency bands in grossular to defects represented
628 by Equations 7-9 is difficult. We tentatively assign the band at 3687-3688 cm⁻¹ to Equation (7),
629 by analogy to the corresponding defect in olivine. This attribution helps to reconcile the H
630 diffusion behavior observed by Kurka et al. (2005), who found that this band and the band at
631 3600 cm⁻¹ decrease more rapidly than bands at 3645 and 3568 cm⁻¹. Specifically, H diffusion of
632 the defect associated with Equation 7 can take place rapidly via the reaction:



636 This reaction is similar to the generalized redox reaction represented by Equation (6) but is
637 defect-specific. In this case, F diffusion – which is inherently slower than H diffusion – is not
638 needed to maintain charge balance because dehydration involves oxidation of Fe²⁺ in the
639 dodecahedral site. Many studies have found that oxidation reactions of this type are faster than
640 reactions that require counter-diffusion of cations to maintain charge balance (Ingrin and

641 Blanchard 2006), and Reynes et al. (2018) provide direct evidence from color changes in
642 dehydrated crystals and experiments at variable f_{O_2} that oxidation of Fe^{2+} plays a key role in
643 dehydration of grossular.

644 The effect of dilute F substitution on local symmetry of the grossular structure is
645 unknown, so it is not straightforward to use group theory to predict how many bands should be
646 present for defects containing more than one O-H bond (Equations 8 and 9). Significant
647 proportions of cations other than Ca and Al in neighboring X and Y sites, such as V or Fe
648 (present in some of the grossular garnets in this study; Table 4), could also shift the frequencies
649 of the O-H bands, because these frequencies largely depend on the masses, ionic radii, and
650 electronic states of the neighboring cations (Burns and Strens 1966; Berry et al. 2007; Geiger and
651 Rossman 2018, 2020a). This effect is likely to be minor but may explain the small shifts up to 3
652 cm^{-1} for some peaks in our curve fits for different grossular spectra. The imperfect correlation of
653 F to the integrated absorbance of the high-frequency bands (Fig. 8a) could be related to the
654 additional presence of F in sites with no OH (e.g., Equation 4), vagaries of the fitting exercise, or
655 perhaps other mechanisms completely unrelated to F – such as the cluster model of Geiger and
656 Rossman (2020a,b) or coupled substitution of H and Ti (Reynes et al. 2020), which we discuss
657 below. Therefore, more work including ab initio calculations is needed to verify our hypothesis
658 that clumped OH-F defects are present in grossular. One attractive feature of our model is that
659 the presence of a significant proportion of defect (8) could partially explain the finding of Cho
660 and Rossman (1993) that H is predominantly present in clusters of two closely spaced protons in
661 GRR1386, and by extension to other class 2b grossular garnets.

662

663 **Low frequency O-H absorption bands**

664 No study has yet offered a satisfactory explanation for all the bands below $\sim 3600\text{ cm}^{-1}$ in
665 class 2a and class 7 grossular (some of the bands are also present in class 5 and 6 grossular;
666 Rossman and Aines 1991). Geiger and Rossman (2020a) assigned the band at 3563 cm^{-1} to a
667 localized "hydroandradite group" consisting of a single $(4\text{H})_{\text{Si}}^{\times}$ adjacent to Fe^{3+} in the octahedral
668 site, based on comparison to the most intense O-H band frequency in andradite IR spectra
669 (Amthauer and Rossman 1998; Geiger and Rossman 2018). Furthermore, they speculated that
670 their model for hydrogrossular clusters could be extended to assign other bands at 3581 and 3594
671 cm^{-1} to different sized hydroandradite clusters. This hypothesis is difficult to assess because the
672 total Fe content in many grossular garnets is too low to accurately determine $\text{Fe}^{2+}/\text{Fe}^{3+}$ using
673 established methods. Our cation assignments (Table 4) based on stoichiometry using the
674 calculation scheme of Locock (2008) indicate that all of the Fe is Fe^{2+} for our garnets with 0.06
675 to 1.8 wt% FeO, but this method for calculating $\text{Fe}^{2+}/\text{Fe}^{3+}$ suffers from considerable uncertainty
676 and Fe^{3+} may also be present.

677 The role of Ti in H incorporation in grossular and andradite was recently studied by
678 Reynes et al. (2020). They proposed coupled substitution of Ti on the Y site and 2H for Si, as
679 follows:

680



682

683 FTIR spectra of the grossular studied by Reynes et al. are unusual compared to most grossular
684 garnets surveyed by Rossman and Aines (1991), containing only three bands at 3546, 3595, and
685 3652 cm^{-1} ; the closest match is to GRR1359, a grossular from a metarodingite in the Gruppo di
686 Voltri, Italy (probably from a similar geologic setting as the rodingite grossular studied by

687 Reynes et al.). Bands at similar frequencies are also present in spectra of the class 2b grossular
688 samples in this study, centered at 3546, 3599, and 3657 cm^{-1} in GRR1386. Therefore, this
689 mechanism may also be important in these garnets, which contain between 0.3 to 0.6 wt% TiO_2
690 (Table 4). The presence of a band at 3652-3657 cm^{-1} related to defect (11) could also partially
691 explain the imperfect correlation of F content to high frequency absorption in Figure 8a.

692 Another possibility is that some of the low frequency bands represent H substitution in
693 dodecahedral and/or octahedral sites via defects such as $(2\text{H})_{\text{Ca}}^{\times}$ or $(3\text{H})_{\text{Al}}^{\times}$, respectively. This
694 attribution could further help to explain the identification of two-proton clusters in GRR1386 by
695 Cho and Rossman (1993), if a large fraction of the H is located in the defects (8), (11), and
696 $(2\text{H})_{\text{Ca}}^{\times}$ combined. Substitution of H via defects such as $(2\text{H})_{\text{Ca}}^{\times}$ would also be consistent with
697 the higher E_a measured for lower frequency O-H bands by Reynes et al. (2018), if dehydration
698 requires counter-diffusion of Ca to take place (as opposed to dehydration via a fast-redox
699 mechanism). Although this hypothesis is highly speculative, DFT calculations for nominally
700 anhydrous minerals to date indicate that the $(4\text{H})_{\text{Si}}^{\times}$ defect gives rise to O-H absorptions at higher
701 frequencies than substitutions involving octahedral cation vacancies. This phenomenon applies
702 to olivine (Balan et al. 2011; Umemoto et al. 2011), enstatite (Balan et al. 2013), wadsleyite
703 (Blanchard et al. 2013), and ringwoodite (Blanchard et al. 2009).

704 In principle, clumped OH-F defects in octahedral or dodecahedral sites are also possible,
705 as are coupled substitution mechanisms like those put forth by Valley et al. (1983) (Equation 5).
706 The intensity of the low-frequency bands in East African grossular also correlates positively with
707 F content (Fig. 8b). By analogy to our argument with the high frequency bands, this might
708 suggest a role for such defects in addition to clumped OH-F in tetrahedral sites. One weakness
709 with this idea is that the presence of isolated, clumped OH-F defects in octahedral or

710 dodecahedral sites would require the presence of Si-F bonds, because all O sites in the garnet
711 structure are shared between the tetrahedral site, two dodecahedral sites, and the octahedral site.
712 As noted by Smyth et al. (1990), there are no known mineral structures in which F bonds directly
713 to tetrahedral Si. However, some NMR studies provide evidence for Si-F bonding in
714 aluminosilicate glasses (e.g., Zeng and Stebbins 2000; Liu and Nekvasil 2002). It is probably
715 more likely that any defect associate involving clumped OH-F in an octahedral or dodecahedral
716 site would be paired with a neighboring defect associate in the tetrahedral site (e.g., three H and
717 one F substituting for Si).

718

719 **Coupled H and F substitution in other garnet compositions**

720 Our model of coupled H and F substitution for Si in grossular likely applies to garnets
721 with other compositions. Data from our 2012 session show strong correlations between ^{16}OH and
722 ^{19}F in 11 spessartine garnets (Fig. 6b), similar to the correlations seen for East African grossular
723 (Fig. 6a). These spessartine garnets have peaks at ~ 3582 , 3595, 3615, 3625, 3640, and 3649 cm^{-1}
724 (Arredondo et al. 2001). Bands at similar frequencies are also present in spectra of a spessartine
725 with up to 3.8 wt% F studied by Smyth et al. (1990). Aines and Rossman (1984) recognized that
726 these six peaks (which can be fit with even more bands) cannot be explained by $(4\text{H})_{\text{Si}}^{\times}$ alone. It
727 is tempting to assign the band at 3595 cm^{-1} (with a shoulder at 3582 cm^{-1}) to $(4\text{H})_{\text{Si}}^{\times}$. The lower
728 frequency compared to katoite or grossular can be explained by the high mass of Mn^{2+}
729 (compared to Ca^{2+}) in the X-site (Geiger and Rossman 2018). However, relative peak heights at
730 3582 and 3595 cm^{-1} vary considerably in garnets from different parts of the pegmatite and in
731 spessartine from the Himalayan Mine (Arredondo et al. 2001), which is not easily reconcilable
732 with a single O-H site being responsible for both bands. Taken together, these observations

733 suggest the possibility that some or all of the bands represent clumped OH-F defects analogous
734 to those we propose for grossular.

735 The presence of high frequency bands in some garnets along the grossular-andradite join
736 (Phichaikamjornwut et al. 2012; Geiger and Rossman 2020a) was already noted. In the
737 supplementary material, we provide IR spectra of a Grs₂₆Adr₇₄ garnet (GRR1830) and a nearly
738 end-member andradite (GRR2103) that we analyzed by SIMS in 2012. GRR1830 has at least
739 eight bands, with peaks at 3560, 3580, 3589, 3617, 3640, 3653, 3660, and 3677 cm⁻¹. The band
740 locations are similar to those in the garnets from Thailand studied by Phichaikamjornwut et al.
741 (2012). The spectrum of GRR2103 is dominated by a strong peak at 3563 cm⁻¹ (with a shoulder
742 at about 3547 cm⁻¹) and has only weak absorbance above 3600 cm⁻¹. Published spectra of other
743 garnets close to end-member andradite also typically do not have these bands (e.g., Amthauer
744 and Rossman 1998; Geiger and Rossman 2018). However, Amthauer and Rossman (1998) noted
745 spectral complexity in a near-end member andradite from Stanley Butte, AZ, USA (GRR1137).
746 Again, the number of bands in GRR1830 and the grossular-andradite garnets studied by
747 Phichaikamjornwut et al. (2012) raises the possibility that some of them represent clumped OH-F
748 defects. This inference is also consistent with SIMS data. Whereas GRR1830 yielded an average
749 ¹⁹F/¹⁸O ratio of 0.191, equivalent to 76 μg/g F, measurements during the same session on
750 GRR2103 yielded ¹⁹F/¹⁸O ratios just barely above the detection limit (<1 μg/g F; Mosenfelder
751 and Rossman 2013a).

752 Coupled H-F substitution is less likely to be important in pyrope, if only because it
753 typically contains significantly lower concentrations of both elements compared to other garnet
754 compositions. Mosenfelder and Rossman (2012) report 0.2 to 10 μg/g F in pyrope garnets from
755 mantle xenoliths that contain up to 135 μg/g H₂O (using the IR calibration of Bell et al. 1995).

756 These xenoliths also contain other phases (olivine, orthopyroxene, and/or clinopyroxene) that
757 can partition much of the available F (Mosenfelder et al. 2011; Mosenfelder and Rossman
758 2013a,b). Nearly end-member pyrope from the Dora Maira massif represents an unusual case; its
759 IR spectra are unlike those of other pyrope-almandine garnets, with sharp peaks at 3602, 3641,
760 3651, and 3662 cm^{-1} (Rossman et al. 1989). As noted above similar bands are present in a pyrope
761 synthesized by Geiger et al. (1991).

762 On the one hand, Lu and Keppler (1997) attributed the bands in Dora Maira pyrope to O-
763 H defects associated with Li and B substitution, based on Li_2O and B_2O_3 concentrations
764 measured by ICP-AES (inductively coupled plasma atomic emission spectroscopy). On the other
765 hand, our attribution of high-frequency bands to clumped OH-F defects is particularly apropos in
766 this case because some Dora Maira garnets contain inclusions of phlogopite with up to 1.6 wt%
767 F as well as other F- and Cl-bearing phases, unequivocally indicating that they formed in a
768 halogen-rich environment (Philippot et al. 1995). Furthermore, SIMS analyses of Dora Maira
769 pyrope by Tenner et al. (2009) – while uncalibrated for F concentration – yielded a $^{19}\text{F}/^{30}\text{Si}$ ratio
770 of 0.215, approximately one order of magnitude higher than ratios measured in pyrope garnets
771 from mantle xenoliths (0.008-0.025). A rough estimate of 30 $\mu\text{g/g}$ F can be derived by
772 comparing to our SIMS data on pyrope (Mosenfelder and Rossman 2012), including MON9
773 from Bell et al. (1995), which was also measured by Tenner et al.

774

775

IMPLICATIONS

776 This work highlights technical advances in analytical methods for F and H that could
777 facilitate future studies using garnets to constrain the activities of H_2O and F-species in fluids in
778 equilibrium with garnet-bearing phase assemblages. The present study – including our new

779 calibration for the IR molar absorption coefficient in grossular – most directly applies to geologic
780 problems in the Earth's crust. However, measurements of trace F and H in garnets from mantle
781 xenoliths may also provide additional constraints on recycling of these elements into the mantle,
782 already a topic of interest addressed by studies of F and H in olivines and pyroxenes.

783 Fine-scale zoning of H in garnets such as those from Asbestos or the garnets studied by
784 Jamtveit and Hervig (1994) or Reynes et al. (2020) is probably best studied using micro-
785 analytical techniques such as SIMS or FTIR conducted with a focal plane array (FPA) detector,
786 which is becoming more widely available (the FPA detector has a higher spatial resolution than
787 normal MCT detectors such as those we used; e.g., Reynes et al. 2020). We have also
788 demonstrated that F can be measured reliably with EPMA at levels down to ~50 $\mu\text{g/g}$, and it
789 should be possible to achieve higher analytical throughput at lower cost with EPMA compared to
790 SIMS. Furthermore, in principle, minimum estimates for F concentrations in garnet could be
791 constrained from FTIR spectra alone, once band assignments for coupled H-F defects are
792 confirmed and controversy over incorporation mechanisms is settled. We expect that theoretical
793 calculations will shed additional light on coupled H-F substitution in garnets and other nominally
794 anhydrous minerals.

795

796 **ACKNOWLEDGMENTS**

797 Financial support for this research is gratefully acknowledged from: NSF grants EAR-
798 0947956 and EAR-1322082 to George Rossman, EAR-1347908 to Jed Mosenfelder, NASA
799 80NSSC19K0959 to Marc Hirschmann, the Gordon and Betty Moore Foundation, and the
800 White Rose Foundation. The manuscript was improved by helpful reviews from Andrew Locock,
801 Jörg Hermann, and an anonymous reviewer. We also thank Yunbin Guan for assistance with

802 SIMS analyses and John Beckett for help operating the gas-mixing 1-atm furnace. Campbell
803 Bridges, Peter Flusser, Robert Gaal, Peter Keller, William Larson, Gary Novak, and Julius
804 Petsch are thanked for providing garnet samples that were used in the work.

805

806 **REFERENCES**

807 Aines, R.D., and Rossman, G.R. (1984) The hydrous component in garnets: pyralospites.

808 American Mineralogist, 69, 116-1126.

809 Allen, F.M., and Buseck, P.R. (1988) XRD, FTIR, and TEM studies of optically anisotropic

810 grossular garnets. American Mineralogist, 73, 568-584.

811 Amthauer, G., and Rossman, G.R. (1998) The hydrous component in andradite garnet. American

812 Mineralogist, 83, 835-840.

813 Andrut, M., Wildner, M., and Beran, A. (2002) The crystal chemistry of birefringent natural

814 uvarovites. Part IV. OH defect incorporation mechanisms in non-cubic garnets derived

815 from polarized IR spectroscopy. European Journal of Mineralogy, 14, 1019-1026.

816 Armstrong, J.T. (1988) Quantitative analysis of silicate and oxide minerals, comparison of

817 Monte Carlo, ZAF and $\phi(\rho z)$ procedures. In D.E. Newbury, Ed. Microbeam analysis, p.

818 239-246. San Francisco Press, San Francisco, CA.

819 Arredondo, E.H., Rossman, G.R., and Lumpkin, G.R. (2001) Hydrogen in spessartine-almandine

820 garnets as a tracer of granitic pegmatite evolution. American Mineralogist, 86, 485-490.

821 Aubaud, C., Withers, A.C., Hirschmann, M., Guan, Y., Leshin, L.A., Mackwell, S., and Bell,

822 D.R. (2007) Intercalibration of FTIR and SIMS for hydrogen measurements in glasses

823 and nominally anhydrous minerals. American Mineralogist, 92, 811-828.

- 824 Balan, E., Refson, K., Blanchard, M., Delattre, S., Lazzeri, M., Ingrin, J., Mauri, F., Wright, K.,
825 and Winkler, B. (2008) Theoretical infrared absorption coefficient of OH groups in
826 minerals. *American Mineralogist*, 93, 950-953.
- 827 Balan, E., Ingrin, J., Delattre, S., Kovacs, I., and Blanchard, M. (2011) Theoretical infrared
828 spectrum of OH-defects in forsterite. *European Journal of Mineralogy*, 23, 285–292.
- 829 Basso, R., Giusta, A.D., and Zefiro, L. (1983) Crystal structure refinement of plazolite: a highly
830 hydrated natural hydrogrossular. *Neues Jahrbuch für Mineralogie Monatshefte*, H.6, 251-
831 258.
- 832 Basso, R., and Cabella, R. (1990) Crystal chemical study of garnets from metarodingites in the
833 Voltri Group metaophilites (Ligurian Alps, Italy). *Neues Jahrbuch für Mineralogie*
834 *Monatshefte*, H.3, 127-136.
- 835 Bell, D. R., and Rossman, G. R. (1992) The distribution of hydroxyl in garnets from the sub-
836 continental mantle of southern Africa. *Contributions to Mineralogy and Petrology*, 111,
837 161-178.
- 838 Bell, D.R., Ihinger, P.D., and Rossman, G.R. (1995) Quantitative analysis of trace OH in garnet
839 and pyroxene. *American Mineralogist*, 80, 465–474.
- 840 Beran, A., and Libowitzky, E. (2006) Water in natural mantle minerals II: olivine, garnet, and
841 accessory minerals. In H. Keppler and J. R. Smyth, Eds., *Water in Nominally Anhydrous*
842 *Minerals*, 62, p. 169-191. *Reviews in Mineralogy and Geochemistry*, Mineralogical
843 Society of America, Chantilly, Virginia.
- 844 Bernini, D., Wiedenbeck, M., Dolejs, D., and Keppler, H. (2012) Partitioning of halogens
845 between mantle minerals and aqueous fluids: implications for the fluid flow regime in
846 subduction zones. *Contributions to Mineralogy and Petrology*, 165, 117-128.

- 847 Berry, A., O'Neill, H.St.C., Hermann, J., and Scott, D.R. (2007) The infrared signature of water
848 associated with trivalent cations in olivine. *Earth and Planetary Science Letters*, 261,
849 134–142.
- 850 Bertie, J.E., and Lan, Z. (1996) Infrared intensities of liquids XX: the intensity of the OH
851 stretching band of liquid water revisited, and the best current values of the optical
852 constants of H₂O(l) at 25 °C between 15,000 and 1 cm⁻¹. *Applied Spectroscopy* 50, 1047-
853 1057. □□□□□□□□
- 854 Beyer, C., Klemme, S., Wiedenbeck, M., Stracke, A., and Vollmer, C. (2012) Fluorine in
855 nominally fluorine-free mantle minerals: Experimental partitioning of F between olivine,
856 orthopyroxene and silicate melts with implications for magmatic processes. *Earth and*
857 *Planetary Science Letters*, 337-338, 1-9.
- 858 Birkett, T.C., and Trzcinski, W.E. (1984) Hydrogarnet: multi-site hydrogen occupancy in the
859 garnet structure. *Canadian Mineralogist*, 22, 675-680.
- 860 Blanchard, M., Balan, E., and Wright, K. (2009) Incorporation of water in iron-free ringwoodite:
861 a first-principles study. *American Mineralogist*, 94, 83–89.
- 862 Blanchard, M., Roberge, M., Balan, E., Fiquet, G., and Bureau, H. (2013) Infrared signatures of
863 OH defects in wadsleyite: A first-principles study. *American Mineralogist*, 98, 2132–
864 2143.
- 865 Blanchard M., Ingrin J., Balan E., Kovács I., and Withers A.C. (2017) Effect of iron and trivalent
866 cations on OH defects in olivine. *American Mineralogist*, 102, 302-311.
- 867 Burdo, R.A., and Morrison, G.H. (1971) Table of atomic and molecular lines for spark source
868 mass spectrometry of complex sample-graphite mixes. Report no. 1670. Materials
869 Science Center, Cornell University, Ithaca, New York.

- 870 Bureau, H., Raepsaet, C., Khodja, H., Carraro, A., and Aubaud, C. (2009) Determination of
871 hydrogen content in geological samples using elastic recoil detection analysis (ERDA).
872 *Geochimica et Cosmochimica Acta* 73, 3311–3322.
- 873 Burns, R.G., and Strens R.G.J. (1966) Infrared study of the hydroxyl bands in clinoamphiboles.
874 *Science*, 153, 890-892
- 875 Chakhmouradian, A.R., Cooper, M.A., Medici, L., Hawthorne, F.C., and Adar, F. (2008)
876 Fluorine-rich hibschite from silicocarbonatite, Afrikanda complex, Russia: crystal
877 chemistry and conditions of crystallization. *Canadian Mineralogist*, 46, 1033-1042.
- 878 Chantler, C.T., Olsen, K., Dragoset, R.A., Chang, J., Kishore, A.R., Kotochigova, S.A., and
879 Zucker, D.S. (2005) X-Ray Form Factor, Attenuation and Scattering Tables (version 2.1).
880 [Online] Available: <http://physics.nist.gov/ffast>. National Institute of Standards and
881 Technology, Gaithersburg, MD.
- 882 Cho, H., and Rossman, G.R. (1993) Single-crystal NMR studies of low-concentration hydrous
883 species in minerals: grossular garnet. *American Mineralogist*, 78, 1149-1164.
- 884 Cohen-Addad, C., Ducros, P., and Bertaut, E.F. (1967) Étude de la substitution du groupement
885 SiO_4 par $(\text{OH})_4$ dans les composés $\text{Al}_2\text{Ca}_3(\text{OH})_{12}$ et $\text{Al}_2\text{Ca}_3(\text{SiO}_4)_{2.16}(\text{OH})_{3.36}$ de type
886 grenat. *Acta Crystallographica*, 23, 220–230.
- 887 Crépisson, C., Blanchard, M., Bureau, H., Sanloup, C., Withers, A.C., Khodja, H., Surble, S.,
888 Raepsaet, C., Beneut, K., Leroy, C., Giura, P., and Balan, E. (2014) Clumped fluoride-
889 hydroxyl defects in forsterite: implications for the upper-mantle. *Earth and Planetary*
890 *Science Letters*, 390, 287–295.

- 891 Dalou, C., Koga, K.T., Shimizu, N., Boulon, J., and Devidal, J.L. (2012) Experimental
892 determination of F and Cl partitioning between lherzolite and basaltic melt. Contributions
893 to Mineralogy and Petrology, 163, 591-609.
- 894 Donovan, J.J., Lowers, H.A., and Rusk, B.G. (2011) Improved electron probe microanalysis of
895 trace elements in quartz. American Mineralogist, 96, 274-282.
- 896 Fitzsimons, I.C.W., Harte, B., and Clark, R.M. (2000) SIMS stable isotope measurement:
897 counting statistics and analytical precision. Mineralogical Magazine, 64, 59–83.
- 898 Flohr, M.J.K., and Ross, M. (1989) Alkaline igneous rocks of Magnet Cove, Arkansas:
899 metasomatized ijolite xenoliths from Diamond Jo quarry. American Mineralogist, 74,
900 113-131.
- 901 Geiger, C.A., and Armbruster, T. (1997) $Mn_3Al_2Si_3O_{12}$ spessartine and $Ca_3Al_2Si_3O_{12}$ grossular
902 garnet: dynamical structural and thermodynamic properties. American Mineralogist, 82,
903 740–747.
- 904 Geiger, C.A., and Rossman, G.R. (1994) Crystal field stabilization energies of almandine-pyrope
905 and almandine-spessartine garnets determined by FTIR near infrared measurements.
906 Physics and Chemistry of Minerals, 21, 516-525.
- 907 Geiger, C.A., and Rossman, G.R. (2018) IR spectroscopy and OH⁻ in silicate garnet: the long
908 quest to document the hydrogarnet substitution. American Mineralogist, 103, 384-393.
- 909 Geiger, C.A., and Rossman, G.R. (2020a) Micro- and nano-size hydrogarnet clusters and proton
910 ordering in calcium silicate garnet: Part I. The quest to understand the nature of “water”
911 in garnet continues. American Mineralogist, 105, 455-467.

- 912 Geiger, C.A., and Rossman, G.R. (2020b) Micro- and nano-size hydrogarnet clusters in calcium
913 silicate garnet: Part II. Mineralogical, petrological, and geochemical aspects. American
914 Mineralogist, 105, 468-478.
- 915 Geiger, C.A., Langer, K., Bell, D.R., Rossman, G.R., and Winkler, B. (1991) The hydroxide
916 component in synthetic pyrope. American Mineralogist, 76, 49–59.
- 917 Geiger, C.A., Stahl, A., and Rossman, G.R. (2000) Single-crystal IR- and UV/ VIS-spectroscopic
918 measurements on transition-metal-bearing pyrope: The incorporation of hydroxide in
919 garnet. European Journal of Mineralogy, 12, 259–271.
- 920 Giuliani, G., Ohnenstetter, D., Palhol, F., Feneyrol, J., Boutroy, E., de Boissezon, H., and
921 Lhomme, T. (2008) Karelianite and vanadian phlogopite from the Merelani Hills gem
922 zoisite deposits, Tanzania. Canadian Mineralogist, 46, 1183-1194.
- 923 Giuliani, G., Fallick, A.E., Feneyrol, J., Ohnenstetter, D., Pardieu, V., and Saul, M. (2011)
924 $^{18}\text{O}/^{16}\text{O}$ and V/Cr ratios in gem tsavorite from the Neoproterozoic Mozambique
925 metamorphic belt: a clue towards their origins? Mineralium Deposita, 46, 671-676.
- 926 Grew, E., Locock, A.J., Mills, S.J., Galuskina, I.O., Galuskin, E.V., and Hålenius, U. (2013)
927 Nomenclature of the garnet supergroup. American Mineralogist, 98, 785-811.
- 928 Grützner, T., Kohn, S.C. Bromiley, D.W., Rohrbach, A., Berndt, J., and Klemme, S. (2017) The
929 storage capacity of fluorine in olivine and pyroxene under upper mantle conditions.
930 Geochimica et Cosmochimica Acta, 208, 160–170.
- 931 Guggino, S.N., and Hervig, R.L. (2011) Synthesis and characterization of five new F-bearing
932 basalt reference materials (Fba glasses): quantifying the fluorine content of the basaltic
933 glass standards BCR-2G, BHVO-2G, GSA-1G, GSC-1G, GSD-1G, GSE-1G, ML3B-G,

- 934 KL2-G, and ALV-519-4. American Geophysical Union, Fall Meeting 2011, abstract
935 #V31C-2535.
- 936 Harmon, K.M., Gabriele, J.M., and Nuttal, A.S. (1982) Hydrogen bonding in the tetrahedral
937 $O_4H_4^{4-}$ cluster in hydrogrossular. *Journal of Molecular Structure*, 82, 213–219.
- 938 Hauri, E.H., Wang, J., Dixon, J.E., King, P.L., Mandeville, C., and Newman, S. (2002) SIMS
939 analysis of volatiles in silicate glasses 1. Calibration, matrix effects and comparisons with
940 FTIR. *Chemical Geology*, 183, 99-114.
- 941 Hervig, R.L., and Bell, D.R. (2005) Fluorine and hydrogen in mantle megacrysts. American
942 Geophysical Union, Fall Meeting 2005, abstract V41A-1426.
- 943 Ingrin, J., and Blanchard, M. (2006) Diffusion of hydrogen in minerals. In H. Keppler and J.R.
944 Smyth, Eds., *Water in Nominally Anhydrous Minerals*, 62, p. 291–320, Reviews in
945 Mineralogy and Geochemistry, Mineralogical Society of America, Chantilly, Virginia.
- 946 Jamtveit, B., and Hervig, R.L. (1994) Constraints on transport and kinetics in hydrothermal
947 systems from zoned garnet crystals. *Science*, 263, 505-508.
- 948 Johnson E. A., and Rossman G. R. (2003) The concentration and speciation of hydrogen in
949 feldspars using FTIR and 1H MAS NMR spectroscopy. *American Mineralogist*, 88, 901–
950 911.
- 951 Johnson E. A., and Rossman G. R. (2004) A survey of hydrous species and concentrations in
952 igneous feldspars. *American Mineralogist*, 89, 586–600.
- 953 Kalinichenko, A.M, Proshko, Y.Ya, Matyash, LV., Pavlishin, V.L, and Gamarnik, M.Ya. (1987)
954 *Geochemistry international*, 24, 132-135.

- 955 Khomenko, V.M., Langer, K., Beran, A., Koch-Müller, M., and Fehr, T. (1994) Titanium
956 substitution and OH-bearing defects in hydrothermally grown pyrope crystals. *Physics
957 and Chemistry of Minerals*, 20, 483-488.
- 958 Klemme, S., and Stalder, R. (2018) Halogens in the Earth's mantle: what we know and what we
959 don't. In D.E. Harlov and L. Aranovich, Eds., *The Role of Halogens in Terrestrial and
960 Extraterrestrial Geochemical Processes*, p. 847-869. Springer, Cham, Switzerland.
- 961 Koga, K., Hauri, E., Hirschmann, M.M., and Bell, D. (2003) Hydrogen concentration analyses
962 using SIMS and FTIR: comparison and calibration for nominally anhydrous minerals.
963 *Geochemistry, Geophysics, and Geosystems*, 4, doi: 10.1029/2002GC000378.
- 964 Kröger, F., and Vink, H. (1956) Relations between the concentrations of imperfections in
965 crystalline solids. In F. Seitz and D. Turnbull, Eds., *Solid state physics*, 3. Elsevier,
966 Amsterdam, pp. 307-435.
- 967 Kurka, A., Blanchard, M., and Ingrin, J. (2005) Kinetics of hydrogen extraction and deuteration
968 in grossular. *Mineralogical Magazine*, 69, 359–371.
- 969 Lager, G.A., Armbruster, T., and Faber, G. (1987) Neutron and X-ray diffraction study of
970 hydrogarnet $\text{Ca}_3\text{Al}_2(\text{OH}_4)_3$. *American Mineralogist*, 72, 756–765.
- 971 Lager, G.A., Armbruster, T., Rotella, F.J., and Rossman G.R. (1989) OH substitution in garnets:
972 X-ray and neutron diffraction, infrared, and geometric-modeling studies. *American
973 Mineralogist* 74, 840–851.
- 974 Libowitzky, E., and Beran, A. (1995) OH defects in forsterite. *Physics and Chemistry of
975 Minerals*, 22, 387–392.
- 976 Libowitzky, E., and Rossman, G.R. (1997) An IR absorption calibration for water in minerals.
977 *American Mineralogist*, 82, 1111-1115.

- 978 Liu, Y., and Nekvasil, H. (2002) Si-F bonding in aluminosilicate glasses: Inferences from ab
979 initio NMR calculations. American Mineralogist, 87, 339-346.
- 980 Locock, A.J. (2008) An excel spreadsheet to recast analyses of garnet into end-member
981 components, and a synopsis of the crystal chemistry of natural silicate garnets.
982 Computers and Geosciences, 34, 1769-1780.
- 983 Lu, R., and Keppler, H. (1997) Water solubility in pyrope to 100 kbar. Contributions to
984 Mineralogy and Petrology, 129, 35-42.
- 985 Maldener, J., Hösch, A., Langer, K., and Rauch, F. (2003) Hydrogen in some natural garnets
986 studied by nuclear reaction analysis and vibrational spectroscopy. Physics and Chemistry
987 of Minerals, 30, 337-344.
- 988 Manning, C.E., and Bird, D.K. (1990) Fluorian garnets from the host rocks of the Skaergaard
989 intrusion: implications for metamorphic fluid composition. American Mineralogist, 75,
990 859-873.
- 991 Mosenfelder, J.L., and Rossman, G.R. (2012) Fluorine in the mantle: the role of nominally
992 anhydrous minerals. American Geophysical Union, Fall Meeting 2012, Abstract FDI54A-
993 06.
- 994 Mosenfelder, J.L., and Rossman, G.R. (2013a) Analysis of hydrogen and fluorine in pyroxenes: I.
995 Orthopyroxene. American Mineralogist, 98, 1026-1041.
- 996 Mosenfelder, J.L., and Rossman, G.R. (2013b) Analysis of hydrogen and fluorine in pyroxenes:
997 part II. Clinopyroxene. American Mineralogist, 98, 1042-1054.
- 998 Mosenfelder, J.L., Le Voyer, M., Rossman, G.R., Guan, Y., Bell, D.R., Asimow, P.D., and Eiler,
999 J.M. (2011) Analysis of hydrogen in olivine by SIMS: evaluation of standards and
1000 protocol. American Mineralogist, 96, 1725-1741.

- 1001 Mosenfelder, J.L., Rossman, G.R., and Johnson, E.A. (2015) Hydrous species in feldspars: a
1002 reassessment based on FTIR and SIMS. *American Mineralogist*, 100, 1209-1221.
- 1003 Mosenfelder, J.L., Andrys, J.L., von der Handt, A., Kohlstedt, D.L., and Hirschmann, M.M.
1004 (2020) Hydrogen incorporation in plagioclase. *Geochimica et Cosmochimica Acta*, 277,
1005 87–110.
- 1006 O’Leary, J.A., Rossman, G.R., and Eiler, J.M. (2007) Hydrogen analysis in minerals by
1007 continuous-flow mass spectrometry. *American Mineralogist*, 92, 1990-1997.
- 1008 Paterson, M.S. (1982) The determination of hydroxyl by infrared absorption in quartz, silicate
1009 glasses, and similar materials. *Bulletin de Minéralogie*, 105, 20-29.
- 1010 Phichaikamjornwut, B., Skogby, H., Ounchanum, P., Limtrakun, P., and Boonsoong, A. (2012)
1011 Hydrous components of grossular-andradite garnets from Thailand: thermal stability and
1012 exchange kinetics. *European Journal of Mineralogy*, 24, 107-121.
- 1013 Philippot, P., Chevallier, P., Chopin, C., and Dubessy, J. (1995) Fluid composition and evolution
1014 in coesite-bearing rocks (Dora-Maira massif, Western Alps): implications for element
1015 recycling during subduction. *Contributions to Mineralogy and Petrology*, 121, 29-44.
- 1016 Raepsaet, C., Bureau, H., Khodja, H., Aubaud, C., and Carraro, A. (2008) μ -ERDA
1017 developments in order to improve the water content determination in hydrous and
1018 nominally anhydrous mantle phases. *Nuclear Instruments and Methods in Physics*
1019 *Research Section B: Beam Interactions with Materials and Atoms* 266, 1333–1337.
- 1020 Reynes, J., Jollands, M., Hermann, J., and Ireland, T. (2018) Experimental constraints on
1021 hydrogen diffusion in garnet. *Contributions to Mineralogy and Petrology*, 173, 69.

- 1022 Reynes, J., Lanari, P., and Hermann, J. (2020) A mapping approach for the investigation of Ti–
1023 OH relationships in metamorphic garnet. *Contributions to Mineralogy and Petrology*, 175,
1024 46.
- 1025 Roberge, M., Bureau, H., Bolfan-Casanova, N., Frost, D.J., Raepsaet, C., Surble, S., Khodja, H.,
1026 Auzende, A.-L., Fiquet, G. (2015) Is the transition zone a deep reservoir for fluorine?
1027 *Earth and Planetary Science Letters*, 429, 25-32.
- 1028 Rossman, G.R. (2006) Analytical methods for measuring water in nominally anhydrous minerals.
1029 In H. Keppler and J. R. Smyth, Eds., *Water in Nominally Anhydrous Minerals*, 62, p. 1-
1030 28. *Reviews in Mineralogy and Geochemistry*, Mineralogical Society of America,
1031 Chantilly, Virginia.
- 1032 Rossman, G.R., and Aines, R.D. (1986) Spectroscopy of birefringent grossular from Asbestos,
1033 Quebec, Canada. *American Mineralogist*, 71, 779-780.
- 1034 Rossman, G.R., and Aines, R.D. (1991) The hydrous components in garnets: grossular-
1035 hydrogrossular. *American Mineralogist*, 76, 1153-1164.
- 1036 Rossman, G.R., Beran, A., and Langer, K. (1989) The hydrous component of pyrope from the
1037 Dora Maira Massif, Western Alps. *European Journal of Mineralogy*, 1, 151–154.
- 1038 Schingaro, E., Lacalamita, M., Mesto, E., Ventruti, G., Pedrazzi, G., Ottolini, L., and Scordari., F.
1039 (2016) Crystal chemistry and light elements analysis of Ti-rich garnets. *American*
1040 *Mineralogist*, 101, 371-384.
- 1041 Slack, G.A., and Chrenko, R.M. (1971) Optical absorption of natural garnets from 1000 to 30000
1042 wavenumbers. *Journal of the Optical Society of America*, 61, 1325-1329.

- 1043 Smyth, J.R., Madel, R.E., McCormick, T.C., Munoz, J.L., and Rossman, G.R. (1990) Crystal-
1044 structure refinement of a F-bearing spessartine garnet. *American Mineralogist*, 75, 314-
1045 318.
- 1046 Sykes, D., Rossman, G., Veblen, D., and Grew, E. (1994) Enhanced H and F incorporation in
1047 borian olivine. *American Mineralogist*, 79, 904–908.
- 1048 Tenner, T.J., Hirschmann, M.M., Withers, A.C., and Hervig, R.L. (2009) Hydrogen partitioning
1049 between nominally anhydrous upper mantle minerals and melt between 3 and 5 GPa.
1050 *Chemical Geology*, 262, 42–56.
- 1051 Umemoto K., Wentzcovitch R.M., Hirschmann M.M., Kohlstedt D.L., and Withers A.C. (2011)
1052 A first-principles investigation of hydrous defects and IR frequencies in forsterite: the
1053 case for Si vacancies. *American Mineralogist*. 96, 1475-1479.
- 1054 Valley, J.W., Essene, E.J., and Peacor, D.R. (1983) Fluorine-bearing garnets in Adirondack calc-
1055 silicates. *American Mineralogist*, 68, 444-448.
- 1056 Verma, R.K. (1960) Elasticity of some high-density crystals. *Journal of Geophysical Research* 65,
1057 757-766.
- 1058 Vermeesch, P. (2018) IsoplotR: A free and open toolbox for geochronology. *Geoscience*
1059 *Frontiers*, 9, 1479-1493.
- 1060 Visser, D. (1993) Fluorine-bearing hydrogarnets from Blengsvatn, Bamble sector, South Norway.
1061 *Mineralogy and Petrology*, 47, 209-218.
- 1062 White, W.B., and Moore, R.K. (1972) Interpretation of the spin allowed bands of Fe²⁺ in silicate
1063 garnets. *American Mineralogist*, 57, 1692-1710.
- 1064 Withers, A.C., and Behrens, H. (1999) Temperature-induced changes in the NIR spectra of

- 1065 hydrous albitic and rhyolitic glasses between 300 and 100 K. *Physics and Chemistry of*
1066 *Minerals*, 27, 119-132.
- 1067 Withers, A.C., Wood, B.J., and Carroll, M.R. (1998) The OH content of pyrope at high pressure.
1068 *Chemical Geology*, 147, 161-171.
- 1069 Withers, A.C., Bureau, H., Raepsaet, C., and Hirschmann, M.M. (2012) Calibration of infrared
1070 spectroscopy by elastic recoil detection analysis of H in synthetic olivine. *Chemical*
1071 *Geology*, 334, 92-98.
- 1072 Witter, J.B., and Kuehner, S.M. (2004) A simple empirical method for high-quality electron
1073 microprobe analysis of fluorine at trace levels in Fe-bearing minerals and glasses.
1074 *American Mineralogist*, 89, 57-63.
- 1075 York, D., Evensen, N.M., Martínez, M.L., and De Basebe Delgado, J. (2004) Unified equations
1076 for the slope, intercept, and standard errors of the best straight line. *American Journal of*
1077 *Physics*, 72, 367-375.
- 1078 Yoshino, T. and Vazhakuttiyakam, J. (2018) Fluorine solubility in bridgmanite: A potential
1079 fluorine reservoir in the Earth's mantle. *Earth and Planetary Science Letters*, 504, 106-
1080 114.
- 1081 Zeng, Q., and Stebbins, J.F. (2000) Fluorine sites in aluminosilicate glasses: High resolution ^{19}F
1082 NMR results. *American Mineralogist*, 85, 863–867.
- 1083 Zhang, C., Koepke, J., Wang, L-X., Wolff, P.E., Wilke, S., Stechern, A., Almeev, R., and Holtz,
1084 F. (2016) A practical method for accurate measurement of trace level fluorine in Mg- and
1085 Fe-Bearing minerals and glasses using electron probe microanalysis. *Geostandards and*
1086 *Analytical Research*, doi: 10.1111/j.1751-908X.2015.00390.x.
- 1087

1088

TABLES

1089 **Table 1.** Garnet sample localities and FTIR data

1090 **Table 2.** Results of elastic recoil detection analysis compared to other H calibration techniques

1091 **Table 3.** SIMS data

1092 **Table 4.** EPMA data and calculated garnet end members

1093

FIGURE CAPTIONS

1095

1096 **FIGURE 1.** Representative FTIR spectra for grossular spectral classes 2, 2b, 3, 4, and 7. Class

1097 designations follow Rossman and Aines (1991). Spectra are plotted without baseline correction

1098 and offset from each other for clarity. Spectra in **a** and **b** are normalized to 1 cm; spectra in **c** are

1099 normalized to different thicknesses (as labeled) to facilitate comparison. **(a)** Class 2 (GRR42),

1100 with the strongest peak at 3647 cm^{-1} , and class 2b (GRR1386). Class 2b has peaks below 3620

1101 cm^{-1} that are almost absent in GRR42. Room temperature spectrum of GRR1386 (solid black

1102 curve) is directly overlain by spectrum taken at 77 K (grey dashed curve). **(b)** Class 2b

1103 (GRR732) and class 7 (GRR1122). Although these spectra have bands at similar positions, in

1104 class 7 the dominant peaks are at lower frequencies and the strongest peak is at 3599 cm^{-1} rather

1105 than 3647 cm^{-1} . **(c)** Class 3 and 4 spectra of natural and synthetic grossular garnets. Three

1106 representative spectra of JLM83a are displayed, with integrated absorbances (Ab_{tot}) equal to 691

1107 (dotted line), 1118 (dashed line), and 1526 cm^{-2} (solid line). The spectrum of GRR53 is from the

1108 slice labeled "GRR53B-F" displayed in Figure 6 of Rossman and Aines (1991). Spectra of

1109 synthetic, end-member grossular crystals are from Geiger and Armbruster (1997) and Withers et

1110 al. (1998). Spectral classes 3 and 4 are nominally distinguished by whether the strongest peak is

1111 at 3631 or 3621 cm^{-1} , respectively. Three of these garnets (GRR53, JLM83a, and the grossular

1112 made by Geiger and Armbruster) have strong peaks at 3689, 3677, 3665, and/or 3559 cm^{-1} that
1113 are weak or absent in the other two samples (GRR1537 and the grossular synthesized by Withers
1114 et al.).

1115

1116

1117 **FIGURE 2.** Detailed comparison near the baselines of 77 K and 298 K spectra of GRR1386.

1118 The band at $\sim 3240 \text{ cm}^{-1}$ at 77 K is attributed to frozen H_2O in fluid inclusions. Bands attributed
1119 to structural OH^- groups are off scale. Spectra of liquid water from Bertie and Lan (1996) and ice
1120 from Johnson and Rossman (2003) also plotted for comparison. GRR1386 spectra are
1121 normalized to 1 cm thickness; spectra of ice and water are arbitrarily scaled.

1122

1123 **FIGURE 3.** Raw (uncorrected) H_2O concentrations determined by ERDA for three East African
1124 grossular garnets (GRR732, GRR771, and GRR1756) and blank forsterite (GRR1017), as a
1125 function of integrated absorbance (Abs_{tot}). Solid line is a York regression. Dashed lines represent
1126 95% confidence intervals calculated from *a priori* errors. Equation and mean squared weighted
1127 deviation (MSWD) of the fit are also shown.

1128

1129 **FIGURE 4.** $^{16}\text{OH}/^{18}\text{O}$ data from two SIMS sessions. Error bars not shown are within the symbol
1130 size. Solid lines are York regressions fit to data (circles) on the blank and East African samples
1131 only, with 95% confidence intervals (calculated from *a priori* errors) displayed as dashed curves.
1132 The equation and MSWD for each regression are also displayed in the graphs. **(a)** 2012 data.
1133 Each point represents the average of three to five measurements, with $2s_x$ (sample standard
1134 deviation) error bars displayed for $^{16}\text{OH}/^{18}\text{O}$. **(b)** 2016 data. In this plot, each point represents a

1135 single analysis. Consequently, uncertainties in $^{16}\text{OH}/^{18}\text{O}$ ($2s_{\bar{x}}$, standard error of the mean) are all
1136 within the symbol size in this plot. Some data points are obscured by overlap with other data; all
1137 original data are given in the supplementary material.

1138

1139 **FIGURE 5.** Backscattered electron image of JLM83a after SIMS analysis. H_2O and F
1140 concentrations (in $\mu\text{g/g}$) are displayed above (up and to the left) each SIMS crater (black spot).
1141 Analysis numbers in order of collection are labeled to the lower right of each spot.
1142 The analyses with asterisks (analyses 15-18) were compromised by elevated background $^{16}\text{OH}^-$
1143 and $^{19}\text{F}^-$, as discussed in the text. Cycle profiles (uncalibrated depth profiles) for analyses 12 and
1144 20 are displayed in supplementary Figure S8.

1145

1146 **FIGURE 6.** Correlations between ^{16}OH and ^{19}F for grossular and spessartine. **(a)** SIMS data for
1147 grossular from sessions in 2012 (open symbols) and 2016 (closed symbols). Each symbol
1148 represents a single analysis ($2s_{\bar{x}}$ uncertainties are within the symbol size for each point). Solid
1149 lines are ordinary least-squares (OLS) regressions to data for East African grossular garnets ($r^2 =$
1150 0.98) and multiple analyses on Asbestos grossular JLM83a ($r^2 = 0.99$). Data on JLM83a that were
1151 compromised by contamination (Fig. 5) are not included in this plot. **(b)** Spessartine data from
1152 2012 session. Each data point on this plot represents an average of between four and 11 analyses
1153 for one sample ($2s_x$ uncertainties are within the symbol size). Solid line is an OLS regression (r^2
1154 $= 0.99$) to all of the data.

1155

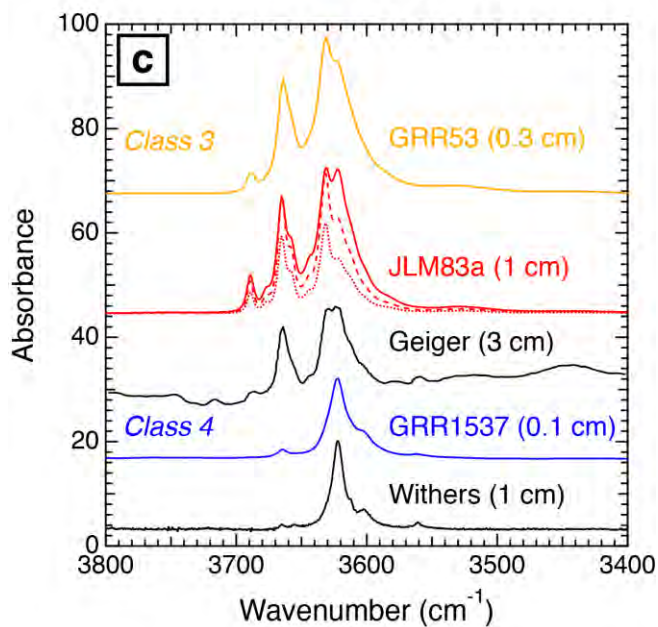
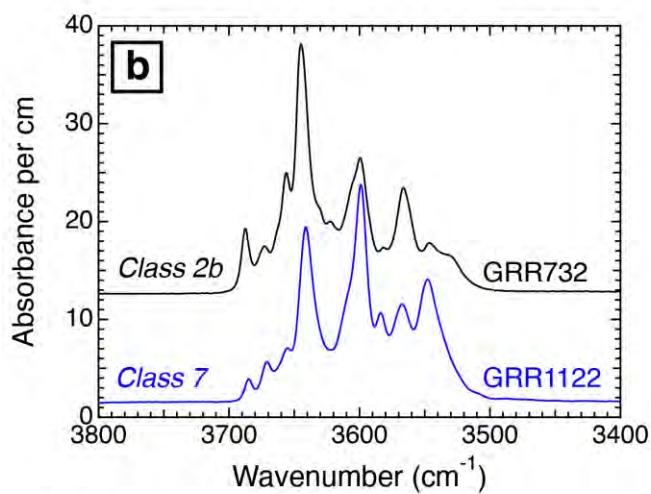
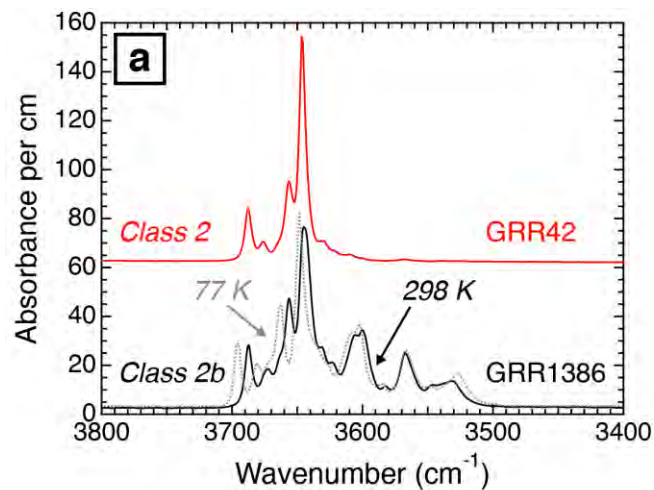
1156

1157 **FIGURE 7.** Comparison of ERDA results (circles) to previous calibration data on Asbestos
1158 grossular (GRR53 and GRR53B, triangles; Aines and Rossman 1984; Rossman and Aines 1991),
1159 Maldener et al. (2003, diamonds), and O'Leary et al. (2007, square). Only two data points from
1160 the compilation of Rossman and Aines (1991) are plotted (for Asbestos garnets GRR53 and
1161 GRR53F), but the original regression determined for their entire data set of grossular and
1162 hydrogrossular garnets over a much wider range of H contents (up to 12.75 wt% H₂O) is
1163 displayed as a dashed line. The ERDA data have been blank corrected in this graph by
1164 subtracting 100 µg/g from the raw values plotted in Figure 3.

1165
1166 **FIGURE 8.** Results of spectral curve fitting plotted as function of calculated F (per formula unit).
1167 Frequencies of fitted bands vary by up to 3 cm⁻¹. Symbols (see inset legend in **a**) correspond to
1168 those in Figure 7. **(a)** Integrated absorbance vs. F for fitted bands centered at ~3631, 3643, 3647,
1169 3657, 3664, 3674, and 3688 cm⁻¹. **(b)** Integrated absorbance vs. F for fitted bands centered at
1170 ~3530, 3539, 3545, 3560, 3567, 3582, 3600, 3608, and 3622 cm⁻¹.

1171
1172
1173
1174
1175
1176
1177
1178
1179
1180

FIGURES



1181

1182 **FIGURE 1.** Representative FTIR spectra for grossular spectral classes 2, 2b, 3, 4, and 7. Class
1183 designations follow Rossman and Aines (1991). Spectra are plotted without baseline correction
1184 and offset from each other for clarity. Spectra in **a** and **b** are normalized to 1 cm; spectra in **c** are
1185 normalized to different thicknesses (as labeled) to facilitate comparison. **(a)** Class 2 (GRR42),
1186 with the strongest peak at 3647 cm^{-1} , and class 2b (GRR1386). Class 2b has peaks below 3620
1187 cm^{-1} that are almost absent in GRR42. Room temperature spectrum of GRR1386 (solid black
1188 curve) is directly overlain by spectrum taken at 77 K (grey dashed curve). **(b)** Class 2b
1189 (GRR732) and class 7 (GRR1122). Although these spectra have bands at similar positions, in
1190 class 7 the dominant peaks are at lower frequencies and the strongest peak is at 3599 cm^{-1} rather
1191 than 3647 cm^{-1} . **(c)** Class 3 and 4 spectra of natural and synthetic grossular garnets. Three
1192 representative spectra of JLM83a are displayed, with integrated absorbances (Ab_{tot}) equal to 691
1193 (dotted line), 1118 (dashed line), and 1526 cm^{-2} (solid line). The spectrum of GRR53 is from the
1194 slice labeled "GRR53B-F" displayed in Figure 6 of Rossman and Aines (1991). Spectra of
1195 synthetic, end-member grossular crystals are from Geiger and Armbruster (1997) and Withers et
1196 al. (1998). Spectral classes 3 and 4 are nominally distinguished by whether the strongest peak is
1197 at 3631 or 3621 cm^{-1} , respectively. Three of these garnets (GRR53, JLM83a, and the grossular
1198 made by Geiger and Armbruster) have strong peaks at 3689, 3677, 3665, and/or 3559 cm^{-1} that
1199 are weak or absent in the other two samples (GRR1537 and the grossular synthesized by Withers
1200 et al.).

1201

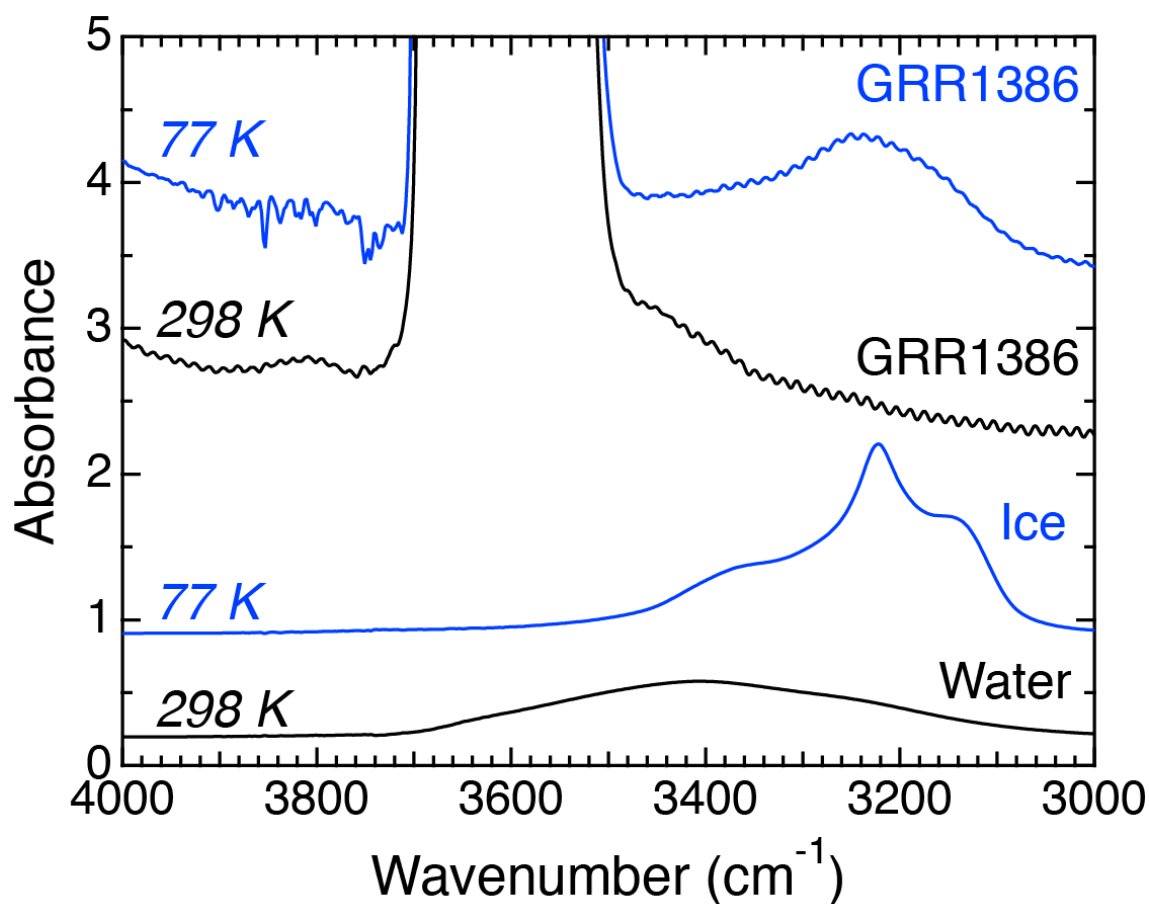
1202

1203

1204

1205

1206



1207

1208 **FIGURE 2.** Detailed comparison near the baselines of 77 K and 298 K spectra of GRR1386.

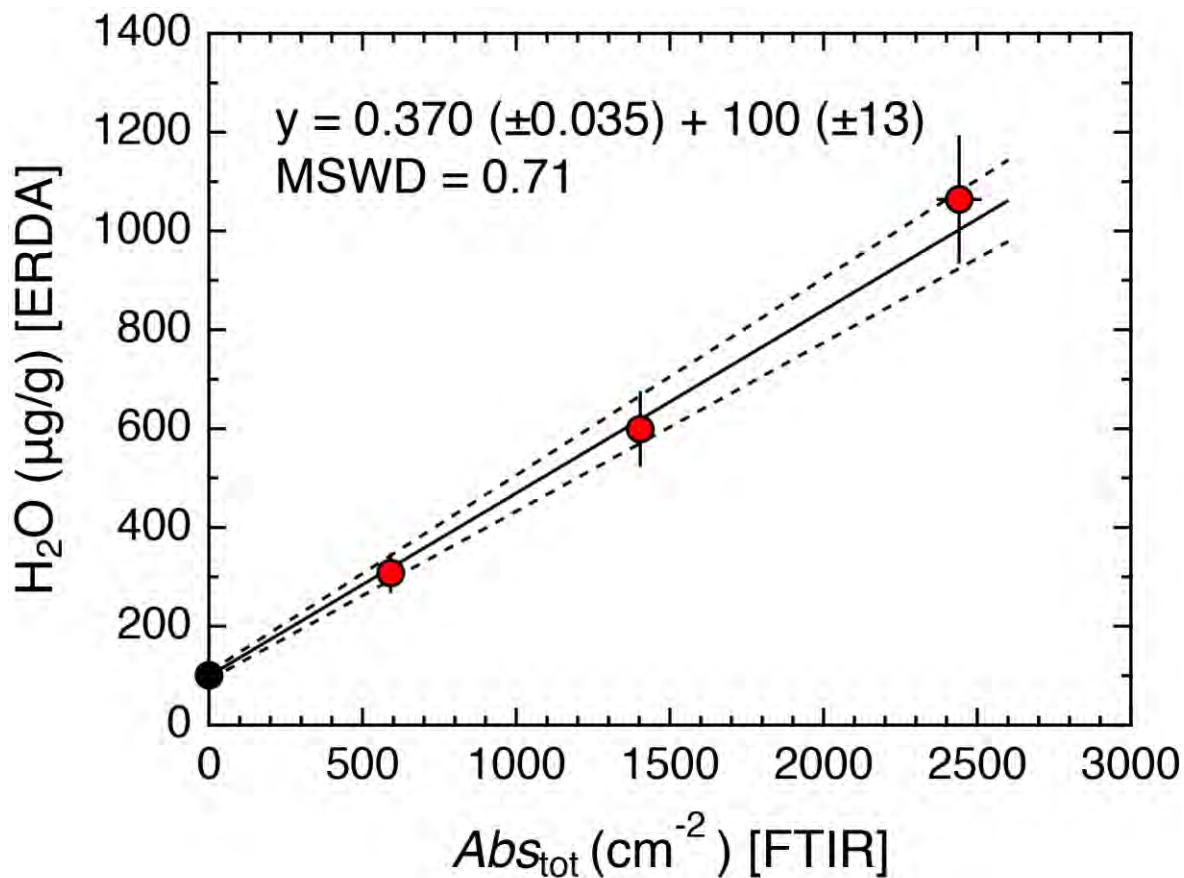
1209 The band at $\sim 3240\text{ cm}^{-1}$ at 77 K is attributed to frozen H_2O in fluid inclusions. Bands attributed

1210 to structural OH^- groups are off scale. Spectra of liquid water from Bertie and Lan (1996) and ice

1211 from Johnson and Rossman (2003) also plotted for comparison. GRR1386 spectra are

1212 normalized to 1 cm thickness; spectra of ice and water are arbitrarily scaled.

1213



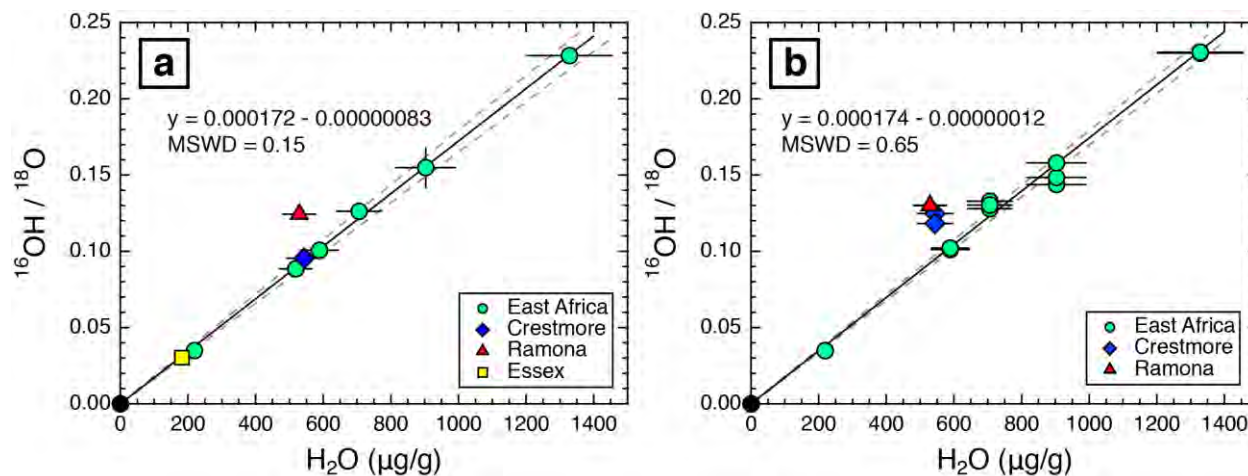
1214
1215 **FIGURE 3.** Raw (uncorrected) H₂O concentrations determined by ERDA for three East African
1216 grossular garnets (GRR732, GRR771, and GRR1756) and blank forsterite (GRR1017), as a
1217 function of integrated absorbance (*Abs_{tot}*). Solid line is a York regression. Dashed lines represent
1218 95% confidence intervals calculated from *a priori* errors. Equation and mean squared weighted
1219 deviation (MSWD) of the fit are also shown.

1220

1221

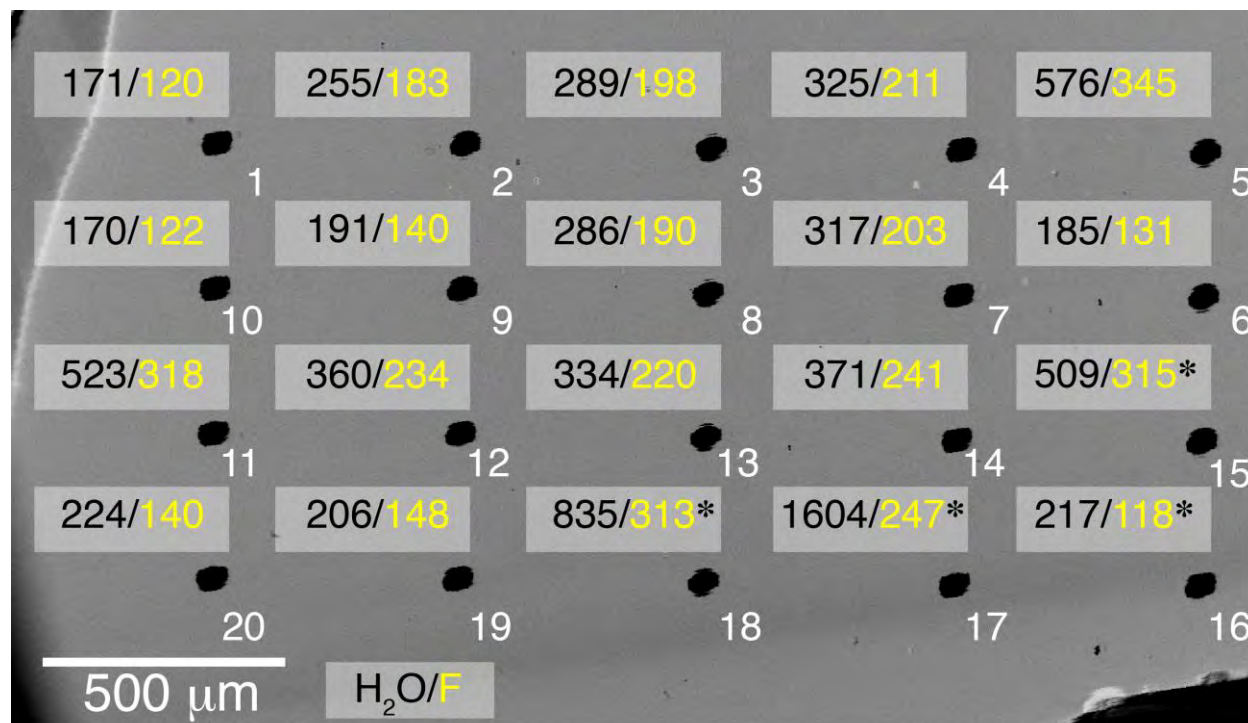
1222

1223

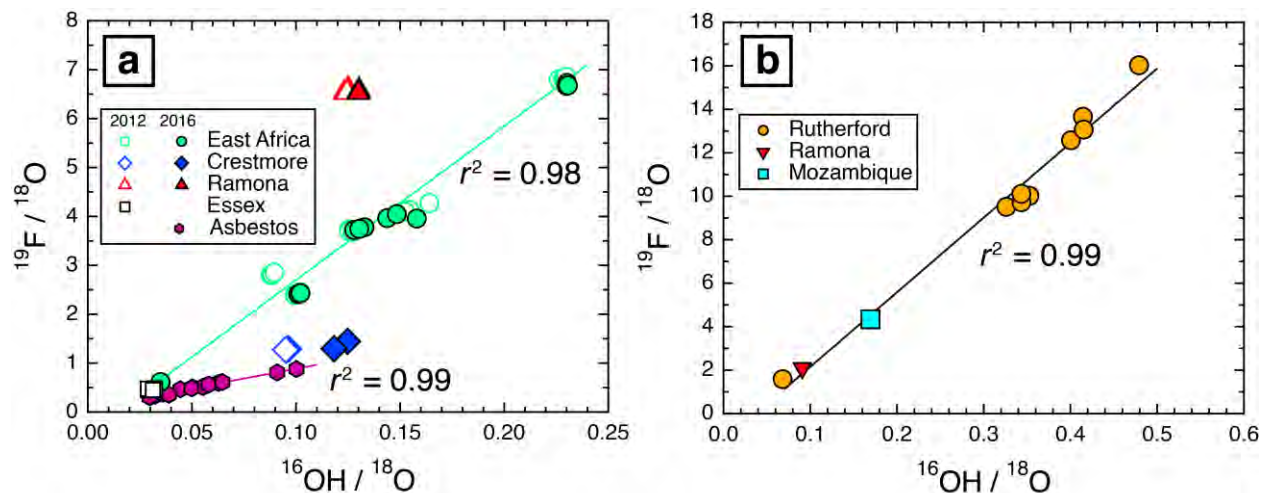


1224
1225 **FIGURE 4.** ¹⁶OH/¹⁸O data from two SIMS sessions. Error bars not shown are within the symbol
1226 size. Solid lines are York regressions fit to data (circles) on the blank and East African samples
1227 only, with 95% confidence intervals (calculated from *a priori* errors) displayed as dashed curves.
1228 The equation and MSWD for each regression are also displayed in the graphs. (a) 2012 data.
1229 Each point represents the average of three to five measurements, with $2s_x$ (sample standard
1230 deviation) error bars displayed for ¹⁶OH/¹⁸O. (b) 2016 data. In this plot, each point represents a
1231 single analysis. Consequently, uncertainties in ¹⁶OH/¹⁸O ($2s_{\bar{x}}$, standard error of the mean) are all
1232 within the symbol size in this plot. Some data points are obscured by overlap with other data; all
1233 original data are given in the supplementary material.

1234
1235
1236
1237
1238
1239
1240

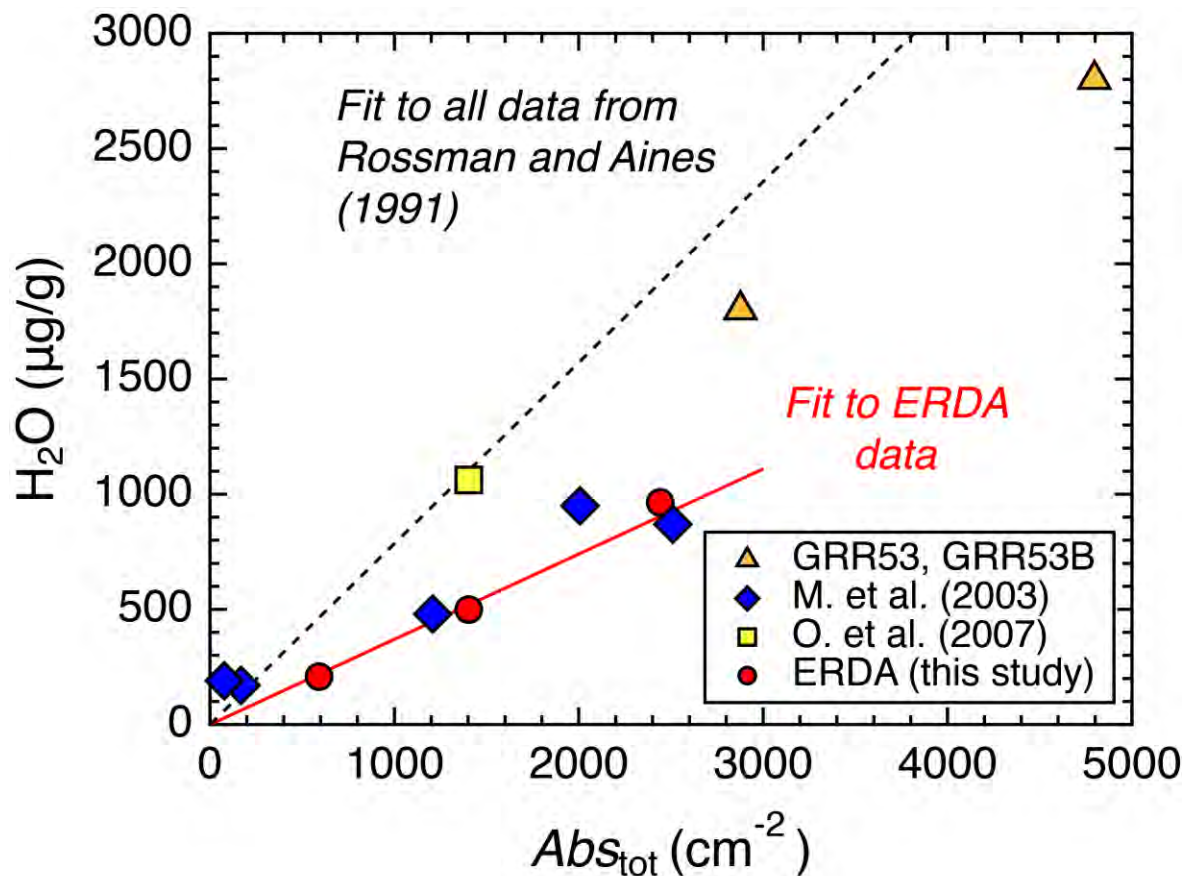


1241
1242 **FIGURE 5.** Backscattered electron image of JLM83a after SIMS analysis. H₂O and F
1243 concentrations (in µg/g) are displayed above (up and to the left) each SIMS crater (black spot).
1244 Analysis numbers in order of collection are labeled to the lower right of each spot.
1245 The analyses with asterisks (analyses 15-18) were compromised by elevated background ¹⁶OH⁻
1246 and ¹⁹F⁻, as discussed in the text. Cycle profiles (uncalibrated depth profiles) for analyses 12 and
1247 20 are displayed in supplementary Figure S8.
1248



1249
1250 **FIGURE 6.** Correlations between ^{16}OH and ^{19}F for grossular and spessartine. (a) SIMS data for
1251 grossular from sessions in 2012 (open symbols) and 2016 (closed symbols). Each symbol
1252 represents a single analysis ($2s_x$ uncertainties are within the symbol size for each point). Solid
1253 lines are ordinary least-squares (OLS) regressions to data for East African grossular garnets ($r^2 =$
1254 0.98) and multiple analyses on Asbestos grossular JLM83a ($r^2 = 0.99$). Data on JLM83a that were
1255 compromised by contamination (Fig. 5) are not included in this plot. (b) Spessartine data from
1256 2012 session. Each data point on this plot represents an average of between four and 11 analyses
1257 for one sample ($2s_x$ uncertainties are within the symbol size). Solid line is an OLS regression (r^2
1258 = 0.99) to all of the data.

1259
1260
1261
1262
1263
1264

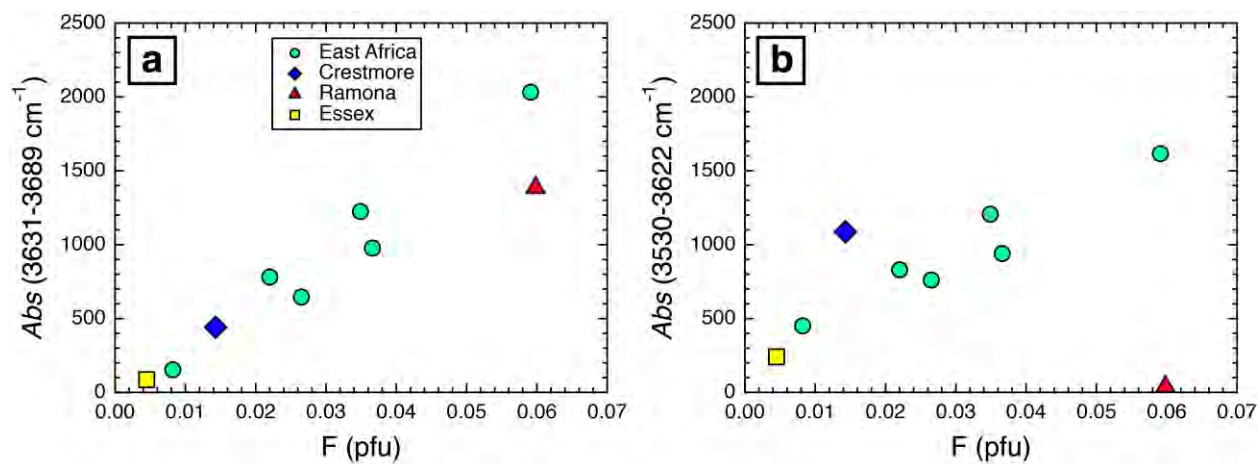


1265
1266 **FIGURE 7.** Comparison of ERDA results (circles) to previous calibration data on Asbestos
1267 grossular (GRR53 and GRR53B, triangles; Aines and Rossman 1984; Rossman and Aines 1991),
1268 Maldener et al. (2003, diamonds), and O'Leary et al. (2007, square). Only two data points from
1269 the compilation of Rossman and Aines (1991) are plotted (for Asbestos garnets GRR53 and
1270 GRR53F), but the original regression determined for their entire data set of grossular and
1271 hydrogrossular garnets over a much wider range of H contents (up to 12.75 wt% H₂O) is
1272 displayed as a dashed line. The ERDA data have been blank corrected in this graph by
1273 subtracting 100 $\mu g/g$ from the raw values plotted in Figure 3.

1274
1275
1276

1277

1278



1279

1280 **FIGURE 8.** Results of spectral curve fitting plotted as function of calculated F (per formula unit).

1281 Frequencies of fitted bands vary by up to 3 cm⁻¹. Symbols (see inset legend in **a**) correspond to

1282 those in Figure 7. **(a)** Integrated absorbance vs. F for fitted bands centered at ~3631, 3643, 3647,

1283 3657, 3664, 3674, and 3688 cm⁻¹. **(b)** Integrated absorbance vs. F for fitted bands centered at

1284 ~3530, 3539, 3545, 3560, 3567, 3582, 3600, 3608, and 3622 cm⁻¹.

1285

1286

1287

1288

1289

Table 1: Garnet sample localities and FTIR data				
Sample No.	Locality	Spectral class^a	Abs_{tot} (cm⁻²)	Mean wavenumber (cm⁻¹)
GRR42	Ramona Mine, California, U.S.A.	2	1430(14)	3647
GRR229	Stream gravel, Merelani Hills, Tanzania	2b	1909(38)	3623
GRR732	Mindi Hills, Kenya	2b	1403(28)	3617
GRR771	Merelani Hills, Tanzania	2b	2441(73)	3622
GRR1122	Crestmore Mine, California, U.S.A.	7	1471(44)	3597
GRR1386	Stream gravel, Merelani Hills, Tanzania	2b	3589(72)	3633
GRR1386a	Stream gravel, Merelani Hills, Tanzania	2b	1592(48)	3619
GRR1429	Essex Country, New York, U.S.A.	7	493(38)	3570-3579 ^b
GRR1756	#2 reef, Scorpion Mine, Voi, Taita, Kenya	7	591(12)	3595
JLM83a	Asbestos, Quebec, Canada	3	691-1544 ^c	3630-3631 ^c
Notes: uncertainties in parentheses are estimated as discussed in text.				
^a Classification scheme of Rossman and Aines (1991)				
^b Range of values for 7 spectra				
^c Range measured in 48 spectra				

Table 2: Results of elastic recoil detection analysis (ERDA) compared to other H calibration techniques

Sample No.	Phase	Abs_{tot} (cm ⁻²)	H ₂ O, µg/g		Reference	Method
			Uncorrected	Blank corrected		
GRR1756	Grossular	591(12)	308(40)	208(40)	This study	ERDA
GRR732	Grossular	1403(28)	599(76)	499(76)	This study	ERDA
			–	1062(31)	1	CFMS
GRR771	Grossular	2441(73)	1064(130)	964(130)	This study	ERDA
NSL1	Rhyolitic glass		11,133(1399)	11,033 (1399)	This study	ERDA
			–	11,600	2	KFT-FTIR
N3	Rhyolitic glass		33,658 (4209)	33,558 (4209)	This study	ERDA
			–	33,000	2	KFT-FTIR
N5	Rhyolitic glass		50,549 (6313)	50,449 (6313)	This study	ERDA
			–	50,600	2	KFT-FTIR
GRR1017 ^a	Forsterite	0	101(14)	0	This study	ERDA
GRR53	Grossular	2877	–	1800	3, 4	MEA, MAN
GRR53F	Grossular	4796	–	2800	4	¹⁹ F NRA
HESS1	Grossular	2510	–	870	5	¹⁵ N NRA
		2006	–	950	5	¹⁵ N NRA
TSAV	Grossular	1208	–	480	5	¹⁵ N NRA
MALI	Grossular	168	–	170	5	¹⁵ N NRA
GRMALI	Grossular	77	–	190	5	¹⁵ N NRA

Notes: References: 1 = O'Leary et al. (2007); 2= Tenner et al. (2009); 3 = Aines and Rossman (1984); 4 = Rossman and A
 CFMS = continuous-flow mass spectrometry; KFT-FTIR = Karl-Fischer titration and FTIR; MEA = P₂O₅ coulometry (mo
 Uncertainties in parentheses are 2s in terms of least units cited

^aBlank reference material used to correct ERDA data.

.ines (1991); 5 = Maldener et al. (2003)

isture evolution analyzer); MAN = evolved H₂ gas volume (manometry); NRA = nuclear reaction analysis

Table 3: SIMS data

Sample no.	SIMS session	No. of analyses	H ₂ O, µg/g ^a	¹⁶ O ¹ H/ ¹⁸ O
GRR1122-HT	2012	4	0	0.000338 – 0.000450 ^c
	2016	3	0	0.001365 – 0.001904 ^c
GRR42	2012	5	529(50)	0.1244(14)
	2016	2 ^d		0.1300, 0.1302
GRR229	2012	4	706(68)	0.1262(16)
	2016	3		0.1304(49)
GRR732	2012	4	519(50)	0.0885(16)
GRR771	2012	4	903(90)	0.155(13)
	2016	3		0.150(15)
GRR1122	2012	4	544(54)	0.0956(12)
	2016	2 ^d		0.1183, 0.1247
GRR1386	2012	4	1328(128)	0.2283(31)
	2016	3		0.2302(6)
GRR1386a	2012	4	589(58)	0.1007(23)
	2016	3		0.1016(10)
GRR1429	2012	4	182(22)	0.0303(34)
GRR1756	2012	4	219(21)	0.0349(2)
	2016	2 ^d		0.349, 0.349 ^d
JLM83a ^e	2016	16 ^f	256-571	0.0296–0.1002

Notes: Numbers in parentheses are 2s uncertainties in terms of least units cited.

^a Values calculated from FTIR using calibration factor of 0.37 (Eq. 1), with uncertainties propagated.

^b Values calculated from ¹⁶O¹H/¹⁸O using working curve for F-bearing glasses.

^c Uncorrected ratios, given as a range.

^d For samples with only two analyses, each analysis is given (separated by comma).

^e Values for this sample are given as a range (for both FTIR and SIMS analyses).

^f Four analyses were rejected owing to a spike in the blank, as described in the text.

$^{19}\text{F}/^{18}\text{O}$	F, $\mu\text{g/g}^b$
1.279(21)	508 (8)
1.325(40)	537(84)
6.563(69)	2606(27)
6.529, 6.584	2559, 2581
3.713(48)	1474(19)
3.751(57)	1470(22)
2.819(49)	1119(19)
4.14(19)	1644(75)
3.99(10)	1565(39)
1.281(16)	508(6)
1.295, 1.447	508, 567
6.824(49)	2709(19)
6.694(64)	2624(25)
2.422(48)	962(19)
2.423(16)	950(6)
0.465(34)	185(13)
0.602(4)	239(2)
0.611, 0.615 ^d	239, 241
0.3502–0.8789	120–345

gated as described in text.

Table 4: EPMA data and calculated garnet end members

Sample No.	GRR42	GRR229	GRR732	GRR771	GRR1122
SiO ₂	38.59(24)	38.77(24)	40.15(39)	39.84(18)	38.69(31)
TiO ₂	–	0.40(3)	0.34(3)	0.54(2)	0.57(6)
Al ₂ O ₃	21.43(12)	20.94(13)	21.97(28)	22.34(8)	17.64(7)
Cr ₂ O ₃	–	0.28(2)	0.04(3)	–	–
V ₂ O ₃	–	1.90(3)	0.88(1)	0.05(2)	–
FeO ^a	3.23(2)	0.08(1)	0.06(3)	0.14(2)	7.53(26)
MnO	0.10(2)	0.90(5)	1.15(1)	0.27(3)	0.38(4)
MgO	–	0.47(2)	0.54(3)	0.34(1)	0.07(2)
CaO	35.33(6)	35.10(14)	35.44(33)	36.25(10)	34.61(20)
H ₂ O ⁺	0.0723 ^b	0.0706 ^c	0.0519 ^c	0.0903 ^c	0.0544 ^c
F	0.2477(36)	0.1516(30)	0.1119 ^c	0.1470(62)	0.0586(62)
O=F	-0.1	-0.06	-0.05	-0.06	-0.02
Total	98.90	99.00	100.68	99.95	99.58
<i>Recalculated</i>					
FeO	1.16	0.08	0.06	0.14	2.09
Fe ₂ O ₃	2.30	–	–	–	6.05
<i>Recalculated Total^f</i>	99.13	99.00	100.68	99.95	100.19
Si	2.9457	2.9576	3.0015	2.9906	2.9804
Ti	–	0.0230	0.0191	0.0305	0.0330
Al ^{VI}	1.8978	1.8583	1.9357	1.9764	1.5924
Al ^{IV}	0.0301	0.0243	–	–	0.0091
Cr	–	0.0169	0.0024	–	–
V	–	0.1162	0.0527	0.0030	–
Fe ²⁺	0.0738	0.0051	0.0038	0.0088	0.1346
Fe ³⁺	0.1324	–	–	–	0.3506
Mn	0.0065	0.0582	0.0728	0.0172	0.0248
Mg	–	0.0534	0.0602	0.0380	0.0080
Ca	2.8896	2.8689	2.8387	2.9155	2.8566
H ₄	0.0092	0.0090	0.0065	0.0113	0.0070
O	11.9402	11.9699	12.0027	11.9959	11.9857
F	0.0598	0.0366	0.0265	0.0349	0.0143
<i>End Members</i>					
Katoite	0.31%	0.30%	0.22%	0.38%	0.23%
FCa garnet	0.50%	0.30%	0.22%	0.29%	0.12%

Schorlomite-Al	—	1.15%	—	—	0.45%
Morimotoite	—	—	—	—	2.40%
Majorite	—	—	—	—	—
Goldmanite	—	5.81%	2.64%	0.15%	—
Uvarovite	—	0.84%	0.12%	—	—
Spessartine	0.22%	1.94%	2.43%	0.57%	0.83%
Pyrope	—	1.78%	2.01%	1.27%	0.27%
Almandine	2.46%	0.17%	0.13%	0.29%	3.69%
Grossular	91.41%	87.22%	91.43%	96.02%	74.49%
Andradite	4.11%	—	—	—	17.53%
Remainder	1.00%	0.48%	0.82%	1.03%	0.00%
Total	100.01%	99.99%	100.02%	100.00%	100.01%

Notes: Cation assignments and garnet end members calculated using Locock (2008), on an 8
 See Locock (2008) for definition of end members. "Remainder" represents the proportion of ca
 Dashed lines denote oxides, elements or end members below detection limit or calculated to b
 EPMA data represent averages (in wt%, with 1 σ uncertainties in parentheses) of 5 to 6 analys

^a Total Fe calculated as FeO.

^b H₂O calculated from 2012 SIMS data, using fit to data for East African grossulars.

^c H₂O calculated from FTIR data (Table 3).

^d H₂O and F based on 2016 SIMS data, for two analyses at extreme ends of range.

^e F based on 2012 SIMS data.

^f Recalculated wt% total after calculation of Fe²⁺/Fe³⁺.

GRR1386	GRR1386a	GRR1429	GRR1756	JLM83a	
				<i>low</i>	<i>high</i>
39.19(23)	39.96(5)	39.48(16)	39.70(11)	39.95(18)	39.95(18)
0.64(3)	0.36(3)	0.42(3)	0.40(1)	–	–
22.29(7)	21.90(5)	18.62(13)	20.90(12)	22.23(13)	22.23(13)
–	–	–	0.29(2)	–	–
–	–	–	1.77(5)	–	–
0.20(3)	1.36(5)	7.27(9)	0.06(1)	1.82(10)	1.82(10)
0.14(2)	0.33(2)	0.21(2)	0.97(1)	0.24(3)	0.24(3)
0.43(1)	0.31(1)	0.14(1)	0.57(1)	–	–
36.27(11)	35.78(6)	34.11(9)	35.02(5)	35.51(14)	35.51(14)
0.1328 ^c	0.0589 ^c	0.0182 ^c	0.0219 ^c	0.0171 ^d	0.0576 ^d
0.2478(24)	0.0924(29)	0.0185 ^c	0.0343(42)	0.012 ^d	0.0345 ^d
-0.10	-0.04	-0.01	-0.01	-0.01	-0.01
99.44	100.11	100.28	99.73	99.77	99.83
0.2	1.36	3.48	0.06	1.82	1.82
–	–	4.22	–	–	–
99.44	100.11	100.71	99.73	99.77	99.83
2.9536	3.0037	3.0137	3.0079	3.0162	3.0138
0.0363	0.0204	0.0241	0.0228	–	–
1.9650	1.9401	1.6752	1.8663	1.9781	1.9765
0.0149	–	–	–	–	–
–	–	–	0.0174	–	–
–	–	–	0.1075	–	–
0.0126	0.0855	0.2219	0.0038	0.1149	0.1148
–	–	0.2422	–	–	–
0.0089	0.0210	0.0136	0.0622	0.0153	0.0153
0.0483	0.0310	0.0022	0.0644	–	–
2.9289	2.8817	2.7899	2.8429	2.8726	2.8703
0.0167	0.0074	0.0023	0.0028	0.0022	0.0072
11.9523	11.9850	11.9955	12.0229	12.0053	12.0031
0.0591	0.0220	0.0045	0.0082	0.0029	0.0082
0.56%	0.25%	0.08%	0.09%	0.07%	0.24%
0.49%	0.18%	0.04%	0.07%	0.02%	0.07%

0.75%	—	—	—	—	—
—	2.04%	2.41%	—	—	—
—	0.37%	0.07%	—	—	—
—	—	—	5.38%	—	—
—	—	—	0.87%	—	—
0.30%	0.70%	0.45%	2.07%	0.51%	0.51%
1.61%	0.66%	—	2.15%	—	—
0.42%	1.78%	6.36%	0.13%	3.64%	3.50%
94.87%	93.43%	76.83%	88.36%	94.66%	94.50%
—	—	12.11%	—	—	—
1.00%	0.59%	1.65%	0.89%	1.10%	1.18%
100.00%	100.00%	100.00%	100.01%	100.00%	100.00%

cation basis (treating H as H_4^{4+}).

ations that could not be allocated.

re 0.

es for all samples except JLM83a (average of 36 analyses).